Energy & Environmental Science

A Thermochemical Study of Iron Aluminate-Based Materials: A Preferred Class for Isothermal Water Splitting

Journal:	*Energy & Environmental Science*
Manuscript ID	EE-ART-08-2021-002679.R2
Article Type:	Paper
Date Submitted by the Author:	13-Dec-2021
Complete List of Authors:	Warren, Kent; University of Colorado Boulder, Department of Chemical and Biological Engineering Tran, Justin; University of Colorado Boulder, Department of Chemical and Biological Engineering Weimer, Alan; University of Colorado Boulder, Department of Chemical and Biological Engineering

A Thermochemical Study of Iron Aluminate-Based Materials: A Preferred Class for Isothermal Water Splitting

Kent J. Warren[a,1,*], Justin T. Tran[a,1], and Alan W. Weimer[a,*]

[a] Department of Chemical and Biological Engineering, University of Colorado, Boulder, Colorado 80309-0596, United States

[1] Contributed equally

[*] Corresponding authors: Email Addresses: kent.warren@colorado.edu, alan.weimer@colorado.edu

Abstract

The use of hydrogen as a renewable fuel has been stymied by our inability to produce it cleanly and economically. The conventional solar thermochemical approach considers a two-step redox cycle with benchmark ceria or a perovskite in a temperature swing configuration, where reduction occurs at a temperature much higher than oxidation. Isothermal redox cycling is feasible and avoids the solid-solid heat recuperation and material stability challenges associated with temperature swing; yet, it has long thought to be inefficient due to the thermodynamic unfavorability of operating the exothermic oxidation reaction at higher temperatures. Here, we show that this setback can be overcome with iron aluminate-based spinel solid solutions that preferentially exhibit large changes in oxygen content within the range of oxygen partial pressures expected in large-scale systems. We explain the experimental results with a defect model that assigns cation – not oxygen – vacancies as the predominant point defect responsible for their superior water-splitting ability. When operated isothermally at 1400 °C, the iron aluminate-based materials demonstrate a capacity for hydrogen production greater than 500 μmol g^{-1} and, as a result, remain viable even under high conversion conditions (i.e., $pO_2 < 500{:}1\ H_2O{:}H_2$), exceeding the hydrogen yields of ceria and two attractive perovskite candidates following a 400 °C (or less) temperature swing. Isothermal water splitting using iron aluminate-based materials opens the door for more simple, robust, and efficient production of renewable hydrogen.

Broader Context

The conversion of intermittent solar energy into chemical fuels, such as hydrogen, can enable widespread access to sustainable feedstocks and dispatchable sources of power, even in regions with insufficient solar insolation. Two-step thermochemical water splitting has long been recognized as a thermodynamically attractive and potentially efficient approach to produce such "solar fuels," as this technology inherently operates at high temperatures and – unlike alternatives that rely on photon-to-electron conversion (e.g., electrolysis) – can harness the entire solar spectrum. Progress towards commercialization, however, has been impeded by the perceived necessity that reduction-oxidation steps must be performed in separate temperature regimes – a consensus driven by material selection and accompanying closed-system analyses that are not representative of practical reactors. Here, we report on the characterization of low-cost iron aluminate-based materials which, under isothermal conditions, were found to exhibit exceptional capacities for hydrogen production, remain viable when exposed to steam diluted with hydrogen, and outperform state-of-the-art fluorite and perovskite candidates following a 400 °C temperature swing. The presented results provide compelling evidence that solar-to-hydrogen conversion with iron aluminate-based materials will be more efficient than the conventional approach, as comparable yields are attainable without incurring excessive energy losses from heating and cooling between redox steps.

1. Introduction

The conversion of intermittent solar radiation into storable and transportable chemical fuels can enable access to sustainable feedstocks and dispatchable sources of power, regardless of geographic location.[1] Of particular interest is technologies that facilitate the endothermic dissociation of H_2O and CO_2 while utilizing heat that is obtained via concentrating optics[2] and/or renewable sources of electricity (e.g., photovoltaics).[3, 4] If coupled with established catalytic processes like Fischer-Tropsch synthesis, product H_2 and CO can be converted to various liquid hydrocarbons (e.g., diesel) and organic oxygenates (e.g., methanol) that are free of nitrogen- and sulfur-containing impurities.[5, 6] For industries that rely on chemical fuels produced through conventional means (i.e., coal gasification, methane reforming, etc.), solar-driven gas-to-liquid technologies offer a viable alternative that can reduce dependence on diminishing fossil energy resources and thus mitigate associated greenhouse gas emissions.[7]

Although direct thermolysis of H_2O (and/or CO_2) is feasible, challenges associated with product separation and low extents of reaction at practicable temperatures (i.e., below 2000 °C[8]) have motivated research into a class of thermochemical cycles, in which a metal oxide facilitates the production of either O_2 or H_2 (and/or CO) via alternating reduction-oxidation (redox) reactions.[9] Figure S1 of the Supporting Information summarizes the thermodynamic implications of using a representative two-step thermochemical cycle to split water. Importantly, bisecting the thermolysis reaction with the introduction of a redox intermediate enables complete reactant conversion in the water-splitting (i.e., oxidation) step at more readily accessible temperatures (e.g., 500 °C); the net reaction is exothermic. Conversely, the removal of oxygen from the oxide (i.e., reduction) is endothermic, and, as a result, increasing the extent of each redox half reaction requires opposite changes in temperature. In practice, implementing a temperature swing between redox regimes imposes significant irreversibilities that arise from sensible heating of the solid, thus resulting in inefficient operation unless heat is recovered via high temperature thermal energy storage.[10] Otherwise, to improve efficiency, recent studies have focused on increasing the extent of reduction at more moderate temperatures (i.e., below 1500 °C), thereby reducing sensible heating demands without compromising the amount of H_2 (and/or CO) produced in the lower-temperature oxidation step. Proposed solutions include (1) integrating auxiliary techniques such as mechanical or thermochemical pumping[11] that, when combined with an inert gas sweep, can further reduce the chemical potential (or partial pressure) of oxygen during reduction or (2) locating a novel redox material – typically a perovskite[12] – with more favorable thermodynamic properties, namely a lower standard partial molar enthalpy of reduction. However, implementing such strategies comes at the expense of either introducing a concomitant energy penalty or further lowering the temperature where oxidation is spontaneous. Rather, traditional closed-system equilibrium analysis indicates that, to decrease the temperature swing between redox regimes, candidate materials should possess higher standard partial molar properties (i.e., both enthalpy and entropy).[13, 14]

In practice, the temperature at which oxidation is performed is not restricted to where the reaction is spontaneous, as thermochemical reactors (i.e., open systems) facilitate continuous product removal from the reaction site. By initiating oxidation at higher temperatures, reaction

kinetics are improved, and if redox regimes are operated isothermally mechanical stresses induced by thermal cycling and challenges associated with implementing solid phase heat recovery can be simultaneously avoided. Although the requirement for sensible heating of process gases increases, the integration of highly effective gas phase heat recovery, as previously demonstrated,[15] can mitigate this otherwise dominant source of irreversibility. Isothermal redox cycling, while it offers several practical advantages, lowers the cyclic capacity of an oxide for the production of H_2 (and/or CO), which in this case is solely dictated by the difference in oxygen chemical potential between the inert sweep gas and high-temperature oxidant.[16] As a result, unlike redox schemes that abide by a temperature swing, material selection is not strictly limited to those that exhibit large enthalpic and entropic changes;[17] rather, materials that preferentially exhibit greater extents of reaction within the attainable range of oxygen chemical potential are more desirable.[18]

In 2013, Muhich et al. introduced cobalt-iron aluminates as a promising class of redox materials for facilitating the isothermal dissociation of H_2O and/or CO_2.[19] The authors used atomic layer deposition (ALD) to coat porous alumina with a thin cobalt ferrite film[20] and under isothermal conditions (i.e., 1350 °C) demonstrated higher hydrogen productivities and yields than observed for water splitting over the established benchmark, nonstoichiometric ceria,[2, 10] after a 350 °C temperature swing. Importantly, the improved performance was consistent, as the presence of cobalt has been suggested to impede the diffusion of iron and thus prevent deactivation by sintering;[21] a later study reported stable performance over 200 cycles.[22] In addition, cobalt has been shown, using in situ X-ray photoelectron spectroscopy, to promote reduction at the cobalt-iron aluminate surface,[23] thereby increasing the thermodynamic driving force for subsequent oxidation. As a result, samples with higher cobalt content, when reduced under equivalent conditions, exhibit faster kinetics for the dissociation of both H_2O[24] and CO_2.[23] However, a trade-off between more rapid kinetics and higher product yields was also observed,[23] such that the largest quantities of H_2 and/or CO are obtained for the oxidation of reduced iron aluminates. Slower kinetics are generally associated with the presence of hercynite ($FeAl_2O_4$),[25, 26] a spinel phase that is only predicted to exist in samples that are cobalt deficient.[24] Although the formation of hercynite can be suppressed with the introduction of other dopants, such as Na_2O and/or MgO,[27] it is worth noting that several studies consider hercynite responsible for the stability of iron aluminates under harsh chemical-looping conditions – conditions where iron oxide rapidly deactivates.[28-30] Unlike inert supports (e.g., ZrO_2) that simply increase diffusion distances as a method to mitigate sintering,[31] the reaction between iron(II) oxide (FeO) and alumina (Al_2O_3) to form hercynite[32] helps resist deactivation by increasing the melting point of the iron aluminate material;[29] FeO and $FeAl_2O_4$ melt at 1377 °C and 1780 °C, respectively. As a result, samples with higher alumina content exhibit more stable performance at the expense of lowering the proportion of redox-active iron.[28]

Despite numerous investigations, research into the mechanism by which iron aluminate-based materials operate, in the context of thermochemical dissociation of H_2O and/or CO_2, has yet to reach a consensus. Early studies[33, 34] referred to this technology as the "hercynite cycle" and proposed that oxygen removal during reduction resulted from the reversible formation of hercynite and cobalt aluminate ($CoAl_2O_4$) spinels at the interface between the cobalt ferrite film and alumina support. Hydrogen production from water splitting was then attributed to stoichiometric

decomposition (or oxidation) of the previously formed spinels. These conclusions were corroborated by ex situ X-ray diffraction[33] and Raman spectroscopy,[34] where the intensity of indicators (i.e., diffraction peak and/or Raman spectra) assigned to hercynite and cobalt ferrite species increased with increasing extent of reduction and oxidation reactions, respectively. However, in a later study, density functional theory calculations invalidated the proposed stoichiometric mechanism, as it was determined that the enthalpy of forming separate spinels during reduction was less than 286 kJ mol^{-1} and thus insufficient for facilitating water splitting.[24] Instead, an oxygen vacancy-mediated mechanism, analogous to how oxides of the fluorite- or perovskite-type are known to operate,[14] was found to possess sufficient endothermicity, thus suggesting that oxygen vacancies may also be responsible for the water-splitting ability of reduced cobalt-iron aluminates. Predictions identified hercynite and a mixed cobalt-iron aluminate compound (e.g., $Co_{0.5}Fe_{0.5}Al_2O_4$) as candidates for accommodating oxygen vacancies, while $CoAl_2O_4$ was found to be incapable of splitting water. To further support the computational analysis, the phases present in an ALD-prepared cobalt-iron aluminate were characterized by in situ high-temperature X-ray diffraction under conditions relevant to the isothermal dissociation of H_2O and/or CO_2.[24] Shifts in the position of the characteristic peak associated with the mixed cobalt-iron aluminate compound were observed, an indication of lattice contraction or expansion that was rationalized by the formation or consumption of oxygen vacancies, respectively. Furthermore, the characteristic peak assigned to cobalt ferrite was not detected in either reducing or oxidizing atmospheres, thereby confirming that, although cobalt ferrite may exist at ambient conditions, it does not directly participate in the production of H_2 and/or CO. This understanding that – depending on the cobalt content – either hercynite or a mixed cobalt-iron aluminate compound is redox active has been adopted in later studies;[23, 35-37] however, there remains debate on the mechanism, with a recent work[35] suggesting that hercynite actually accommodates cation, not oxygen, vacancies.

On the other hand, established phase diagrams of the Fe-Al-O system,[38, 39] for example, suggest that the redox behavior of iron aluminates cannot be solely attributed to hercynite, as phase-pure hercynite is not expected until the surrounding oxygen partial pressure (pO_2) is several orders of magnitude lower than that observed under water-splitting conditions. Instead, for a more appropriate range of pO_2 (i.e., between 10^{-5} and 10^{-3} bar), hercynite exists in solution with other compounds including magnetite (Fe_3O_4) – a well-characterized redox material that accommodates cation vacancies.[40] Notably, the equilibrium composition of this solid solution is dictated by the oxygen fugacity in the gas phase,[25, 26] such that the concentration of magnetite increases with increasing pO_2. As a result, rather than interpret shifts in the diffraction peak position as a consequence of oxygen vacancy formation/consumption,[24] prior studies have considered this measurement an indication of material composition, using it to quantify the proportion of spinels (i.e., Fe_3O_4 and $FeAl_2O_4$) within the solid solution.[25, 28, 41] This discrepancy in the interpretation of X-ray diffraction data and lack of an established reaction mechanism warrants further investigation into characterizing iron aluminate-based materials under conditions relevant to two-step thermochemical fuel production. Therefore, in this study, a comprehensive thermodynamic analysis is developed and coupled with an experimental assessment of the cobalt-iron aluminate compositional space to not only provide mechanistic insight but also enable more extensive comparisons with other candidate redox materials. Ultimately, the results demonstrate that iron

aluminate-based materials exhibit superior performance and remain viable under (less favorable) conditions expected in large-scale systems, where delivering excess oxidant and implementing wide temperature swings are avoided to improve efficiency.[42]

2. Methods

2.1. Experimental

2.1.1. Materials Synthesis and Chemical Characterization

The following recipe was used to synthesize three compound formulations within the cobalt-iron aluminate ($Co_xFe_{1-x+y}Al_{2-y}O_4$) compositional space: (1) x = 0.40 and y = 0, (2) x = 0 and y = 0, and (3) x = 0 and y = 0.40. For brevity, and to avoid implying the existence of a particular phase, these formulations are hereafter referred to as Co13Fe20Al67, Fe33Al67, and Fe47Al53, respectively. The methods outlined in this recipe were specifically tailored to ensure that the preparation of Fe33Al67 yielded high-purity hercynite, which is conventionally achieved by subjecting homogeneous precursor mixtures of the proper cation ratio (i.e., 33 mol% Fe) to prolonged thermal treatments at high temperatures and low oxygen partial pressures.[43] To homogeneously disperse metal cations, prior studies have considered – for example – mechanical mixing of Fe_2O_3 and Al_2O_3 powders,[44] decomposing Fe and Al ammonium alums in solution,[38] or physically combining metallic Fe with dehydrated $Al(OH)_3$.[45] Here, however, a modified Pechini sol-gel method,[46] commonly used in the synthesis of perovskites,[47] was leveraged to ensure that cations were uniformly dispersed before calcination. First, using thermogravimetric analysis (NETZSCH, STA 449 F1 Jupiter), representative samples of $Co(NO_3)_2 \cdot 6H_2O$, $Fe(NO_3)_3 \cdot 9H_2O$, and $Al(NO_3)_3 \cdot 9H_2O$ (Sigma-Aldrich, ACS reagent, ≥ 98%) were dehydrated to identify the nominal wt. % of metal cations. Stoichiometric amounts of these metal nitrates, as prescribed by the desired cation ratio of each formulation, were then dissolved with dry citric acid monohydrate ($C_6H_8O_7 \cdot H_2O$, Fisher Scientific, Certified ACS) in 20 mL of deionized (DI) water. The molar ratio of $C_6H_8O_7 \cdot H_2O$ to total metal cations was set to 3:2.[48, 49] The aqueous solution, contained within a glass beaker, was continuously stirred at 300 RPM for 2 hours under ambient conditions. Then, ethylene glycol ($C_2H_6O_2$, Fisher Scientific, Certified) was introduced at a ratio of 2 moles $C_2H_6O_2$ per mole $C_6H_8O_7 \cdot H_2O$ to further promote homogeneity.[50] After 10 minutes, the solution was slowly heated to 90 °C, where temperature was maintained until complete gelification was attained; the rotation speed of the magnetic stirrer was progressively increased from 300 to 900 RPM during heating. After cooling, easily accessible material was transferred to two alumina combustion boats and air dried at 300 °C for 3 hours in a Lindberg Hevi-Duty tube furnace. Any remaining material adhered to the glass beaker surface was air dried in a drying oven (Fisher Scientific, Isotemp 737F) at 100 °C overnight. The resulting material was separated by formulation and drying approach and then ground with a mortar and pestle into a fine powder.

Thermal treatment consisted of three steps. First, each batch was reinserted into the Lindberg Hevi-Duty tube furnace and individually calcined in air at 850 °C for 24 hours to (1) pyrolyze any remaining organics and (2) form solid solutions that are primarily composed of binary metal oxides. Next, as advised by Woodland and Wood,[45] each solid solution was subsequently reduced to ensure that all components were of the spinel phase. Otherwise, the

authors observed the persistence of impurities (e.g., metallic Fe or corundum) in the final product, in their case, synthetic hercynite. Here, reduction was performed for 6 hours at 900 °C and a pO_2 of approximately 10^{-14} bar. Lastly, each batch was subjected to a 24-hour calcination at 1380 °C and a pO_2 of approximately 10^{-10} bar; these conditions were selected with the intention of promoting the formation of hercynite. A portion of the resulting iron aluminate-based spinels were uniaxially cold-pressed at 2 tons for 120 seconds to form dense cylindrical pellets with the following dimensions: 6 mm diameter, 1–2 mm height, and 50–65 mg mass.

The last two reduction steps were conducted in a stagnation flow reactor,[21] a device well suited for ensuring that samples experience a uniform gas composition. Here, the pO_2 of the system was accurately controlled by delivering a 15 % CO/Ar mixture (Airgas, certified standard) with CO_2 (Airgas, grade 5.0) at different flow rates. By assuming equilibrium of CO_2 thermolysis (i.e., $CO_2 \leftrightarrow CO + ½O_2$), the pO_2 of the atmosphere surrounding the sample is determined according to Equation 1.[51]

$$\frac{pO_2}{P^\circ} = \left(K_r(T)\frac{pCO_2}{pCO}\right)^2 = \left(\frac{K_{CO}(T)\,\dot{F}_{CO_2}}{K_{CO_2}(T)\,\dot{F}_{CO}}\right)^2 \quad (1)$$

Equilibrium constants for the formation of CO_2 and CO (i.e., K_{CO_2} and K_{CO}, respectively) were obtained from NIST-JANAF thermochemical tables as a function of temperature (T);[52] P° is the standard pressure of 1 bar. Inlet mass flow rates of CO_2 and CO (i.e., $\dot{F}_{CO_2}$ and $\dot{F}_{CO}$, respectively) were standardized to 0 °C and 760 Torr. For calcination at 900 °C and 1380 °C, the inlet CO_2/CO ratio was 11.5:1[38] and 1:4, respectively.

The iron aluminate-based materials were characterized by several techniques at different stages of the calcination process and after the experimental campaign. Powder X-ray diffraction (PXRD) was performed on a Bruker D8 Advance diffractometer equipped with a LYNXEYE XE-T detector and monochromatic Cu-Kα radiation; the generator voltage and tube current were 40 kV and 40 mA, respectively. The PXRD patterns were recorded at room temperature between 15° and 100° (2Θ) with a scan rate of 2° min^{-1}, step size of 0.007°, and time per step of approximately 40 s. Each measurement was processed with DIFFRAC.EVA software (Bruker AXS), which was employed to (1) conduct phase identification using reference patterns derived from the Crystallography Open Database (COD)[53] and (2) correct for background effects observed at low diffraction angles (i.e., $2\Theta < 20°$) that are introduced by the PMMA specimen holder. The Fe33Al67 and Fe47Al53 PXRD patterns were further analyzed with FullProf Suite software to enable accurate quantification of phase proportions. The peak profiles were modelled using COD standards and a pseudo-Voigt function, and the refined parameters included scale factor, atomic positions, occupancies, isotropic atomic displacement parameters, and lattice parameters. Scanning electron microscopy (SEM) and energy-dispersive X-ray spectroscopy (EDS) were performed using an FEI Nova NanoSEM 450 equipped with a silicon drift detector (Oxford Instruments, X-Max^N), which enabled morphological surface imaging and qualitative assessment of surface element homogeneity. The respective elemental compositions of the as-synthesized samples were quantified with inductively coupled plasma-optical emission spectrometry (ICP-OES) using an Avio 500 (Perkin Elmer). Prior to analysis, 100 mg powdered samples were

subjected to microwave-assisted acid digestion (CEM Corporation, Discover SP-D 80), where complete dissolution was achieved with a combination of HCl, HNO_3, and HF (Fisher Chemical, TraceMetal™ Grade). To complex excess HF, a saturated solution of H_3BO_3 (Thermo Fisher Scientific, Trace Metal Basis) in ultrapure DI water (ELGA LabWater, PURELAB flex 2) was subsequently introduced into the digested solution, followed by further dilution with additional DI water until the concentration of total dissolved solids was less than 1000 mg L^{-1}.

2.1.2. Thermal Analysis

The equilibrium behavior of the pelletized, iron aluminate-based samples was evaluated using a STA 449 F1 Jupiter thermal analyzer equipped with a vertically oriented sample carrier that enabled thermogravimetric (TG) measurements. A type S thermocouple, imbedded within the TG sample carrier, provided temperature measurements at the location of the sample (T_s). The exposed thermocouple junction directly supported a flat-plate alumina crucible, which was selected to reduce external mass transfer limitations to the pellets; a 6 mm sapphire disc was implemented between each pellet and crucible to prevent any interaction. Upstream of the sample chamber, O_2/Ar mixtures, which contained either 10% O_2 (Airgas, certified standard) or 0.2% O_2 (Airgas, certified standard), were diluted with additional Ar (Airgas, grade 5.0) via two electronic mass flow controllers (Bronkhorst, El-FLOW select) and a manual rotameter (Vögtlin Instruments, Q-Flow 140). Before initiating the experimental campaign, all flow controllers were calibrated (Mesa Labs, FlexCal Series) to ensure accurate delivery of the inlet gases (standardized to 25 °C and 760 Torr) and thus control the pO_2 within the sufficiently mixed sample chamber and hermetically sealed system. Regardless of flow configuration, the total volumetric flow rate (V_{tot}) was maintained at approximately 180 sccm, while the total pressure within the sample chamber remained at one atmosphere (i.e., ~630 Torr for Boulder, Colorado), as outlet gases were exhausted to the ambient. Atmospheric pressure was recorded over the course of each experiment by referencing the measurements reported at the nearby Boulder Municipal Airport, courtesy of the National Weather Service. Any changes in product composition due to oxygen evolution or consumption were qualitatively monitored downstream of the reaction zone with a quadrupole mass spectrometer (NETZSCH, QMS 403C Aëolos).

Before each experiment, the pellets were fully oxidized at either 700 °C or 1100 °C and a pO_2 of approximately 10^{-2} bar; preliminary tests confirmed that complete oxidation was achieved under these conditions, as denoted by the lack of mass gain and stabilization of the oxygen signal gradient. Experiments were then performed at a constant pO_2 between 10^{-2} bar and 10^{-5} bar, and as a result, any relative change in the sample mass was directly imposed by heating or cooling to a different furnace reference temperature (T_{ref}); the rate of heating and cooling between T_{ref} was less than or equal to 15 °C min^{-1}, and T_s never deviated more than 6 °C from T_{ref}. This experimental procedure consisted of evaluating randomly selected T_{ref} from 1000 °C to 1400 °C (in 100 °C increments), where the duration of each isotherm was held for either 1 or 2 hours. For each experiment, samples were subjected to the aforementioned T_{ref} sequence twice, where each sequence was uniquely randomized. In addition, 700 °C isotherms were implemented at the initiation and completion of the overall experiment, as well as in between the two T_{ref} arrays. These lower temperature segments provided a temporal frame of reference for the higher-temperature,

mass-relaxation tests, where greater amounts of oxygen evolution were expected for the considered pO_2 range. If the relative change in sample mass did not equilibrate within the allotted duration, a separate experiment was performed with elongated reactions to ensure thermodynamic equilibrium was attained for all temperatures. Here, the randomized temperature sequences were modified so that samples were only evaluated where equilibrium was not previously established. In these instances, the T_{ref} sequences were organized in ascending order. Regardless of method, to compensate for undesired buoyancy effects observed in the TG measurements, each experiment was immediately replicated in the absence of any reactive material.

2.2. Computational

2.2.1. Phase Equilibria

A thermodynamic analysis of the Fe-Al-O and Co-Fe-Al-O systems was performed using the software package FactSage[54] (version 8.0) to calculate phase equilibria based on the principle of Gibbs free energy minimization. The calculations considered both solution (i.e., slag, corundum, spinel, and monoxide) and pure compound (i.e., gas and solid) databases, and each system was evaluated at a constant pressure (760 Torr) for different cation compositions (ζ), temperatures, and oxygen partial pressures.

2.2.2. Thermodynamic Properties

A defect model, presented in Section 3.1., was proposed to supplement the thermogravimetric measurements by providing insight into material behavior outside the range of conditions examined experimentally. Importantly, describing the effect of T and pO_2 on equilibrium is feasible with knowledge of only a few parameters, namely the standard molar enthalpy (ΔH°) and entropy (ΔS°) of relevant defect reactions. Herein, these thermodynamic state quantities were obtained by minimizing the sum of squared errors (SSE), as defined in Equation 2, between the model predictions and experimental results.

$$\mathrm{SSE} = \sum_{T_{ref}} \sum_{pO_2} (\delta_{model} - \delta)^2 \tag{2}$$

Comparisons were evaluated in terms of the degree of nonstoichiometry (δ), which for the latter is defined, according to Equation 3, as the product of the molar mass ratio of spinel (M_{st}) to oxygen (M_O) and the measured relative change in mass (m) between the equilibrium and stoichiometric states (denoted by subscripts eq and st, respectively) of the spinel. Further details are provided in Section S.2 of the Supporting Information.

$$\delta = \frac{3M_{st}}{4M_O}\left(\frac{m_{eq} - m_{st}}{m_{st}}\right) \tag{3}$$

Note that, in this study, equilibrium was considered established only if (1) the furnace was set at an isothermal condition and (2) the change in mass with respect to time was less than a tenth of a microgram per minute. These criteria are mathematically represented in Equation 4.

$$t_{eq} = t \text{ if } \frac{dT_{ref}(t)}{dt} = 0 \left(^{\circ}\text{C min}^{-1}\right) \text{ and } \left|\frac{dm(t)}{dt}\right| < 0.1 \left(\mu\text{g min}^{-1}\right) \quad (4)$$

Close agreement between theory and experiment, in addition to providing support for the proposed mechanism, allows for the determination of δ at any condition where the defect model assumptions remain valid. As a result, the range in which composition-dependent properties, such as the standard partial molar enthalpy ($\Delta\bar{h}_v^{\circ}$) and entropy ($\Delta\bar{s}_v^{\circ}$) of vacancy formation or consumption, are described is not limited by the scope of the experimental campaign. A thorough delineation of these thermodynamic state functions, in particular, is important, as according to Equation 5 $\Delta\bar{h}_v^{\circ}$ and $\Delta\bar{s}_v^{\circ}$ enable the equilibrium extent of reaction to be determined for a given T and $p\text{O}_2$ (i.e., without requiring explicit knowledge of the defect chemistry).

$$\frac{3}{4}\left(\Delta\bar{h}_v^{\circ}(\delta) - T\Delta\bar{s}_v^{\circ}(\delta)\right) = -\frac{1}{2}RT\ln\left(\frac{p\text{O}_2}{P^{\circ}}\right) \quad (5)$$

Obtaining these properties involves manipulating Equation 5 into the linear form of the van't Hoff equation, plotting $-\ln(\sqrt{p\text{O}^2/P^{\circ}})$ versus $1/T$, and calculating the slope and intercept of the regression line as a function of composition (i.e., δ); note that if the plots exhibit a linear relationship, $\Delta\bar{h}_v^{\circ}$ and $\Delta\bar{s}_v^{\circ}$ can be assumed independent of temperature. For further details, the reader is referred to previous studies[49, 55] where the derivation of an equation analogous to Equation 5 is presented and the approach, although tailored to oxides that accommodate oxygen vacancies, remains relevant for the materials considered herein. The key assumptions underlying this derivation include ideal gas behavior and unity activity of the solid as the change in δ approaches zero.

2.2.3. Water Splitting

The effectiveness of an oxide for facilitating thermochemical water splitting is measured by the change in the extent of reaction (i.e., $\Delta\delta$) that is achieved between reduction and oxidation steps. To predict $\Delta\delta$, which is proportional to the cyclic amount of oxygen and hydrogen evolved from the oxide, one must first establish the attainable operating conditions of each step, particularly the $p\text{O}_2$, as T is independently controlled. At ambient pressure (i.e., 1 bar), the inlet $p\text{O}_2$ of the reduction reaction is defined by the oxygen content in the inert sweep gas, which is typically below 10 ppm. Conversely, the inlet $p\text{O}_2$ of the oxidation reaction is determined according to the temperature-dependent equilibrium of water thermolysis (i.e., $\text{H}_2\text{O} \leftrightarrow \text{H}_2 + \frac{1}{2}\text{O}_2$).[51] Assuming an ideal gas mixture, analogous to Equation 1, the equilibrium constant for the formation of H_2O (i.e., $K_{\text{H}_2\text{O}}$) may be related to the partial pressures of participating gases as shown in Equation 6.[18]

$$\frac{1}{K_{\text{H}_2\text{O}}(T)} = \frac{p\text{H}_2}{p\text{H}_2\text{O}}\left(\frac{p\text{O}_2}{P^{\circ}}\right)^{1/2} = \frac{n_{i,\text{H}_2} + \varepsilon}{n_{i,\text{H}_2\text{O}} - \varepsilon}\left(\frac{\frac{1}{2}\varepsilon}{n_{i,\text{H}_2} + n_{i,\text{H}_2\text{O}} + \frac{1}{2}\varepsilon}\frac{P}{P^{\circ}}\right)^{1/2} \quad (6)$$

Here, the reaction coordinate (ε) was introduced in order to obtain a unique solution for $p\text{O}_2$, provided that the initial number of moles of each species (n_i) and the independent reaction conditions (i.e., T and P) are specified;[56] $K_{\text{H}_2\text{O}}$ was obtained from NIST-JANAF thermochemical tables.[52] Note that in an open system, where any oxygen or hydrogen evolved from the oxide is

swept away, at equilibrium, the pO_2 at the inlet and outlet of either reaction chamber is constant. In this limit, for a particular set of reduction conditions (i.e., T and pO_2), the thermodynamic capacity of an oxide for the production of hydrogen can be quantified solely as a function of oxidation temperature, as the value of pO_2 calculated from Equation 6 is entirely temperature-dependent when only steam is introduced into the system (i.e., $n_{i,H_2} = 0$).[18] It is arguably more relevant, however, to consider how – in practice – reactors are expected to operate in a mass-transfer-limited regime, such that some of the active material may encounter inlet steam diluted with hydrogen produced elsewhere (i.e., $H_2O:H_2 < \infty$). Therefore, using Equation 6, the influence of H_2 on the equilibrium extent of oxidation was also assessed by calculating the corresponding pO_2 of water thermolysis including some quantity of H_2 (i.e., $n_{i,H_2} > 0$). Regardless of the input steam-to-hydrogen ratio, considering the aforementioned assumptions, predicting $\Delta\delta$ for an oxide simply involves (1) locating the equilibrium extents of reduction and oxidation (i.e., δ_{red} and δ_{ox}, respectively) at the established operating conditions and (2) determining their difference.

3. Results and Discussion

3.1. Mechanistic Insight and Defect Model Development

The X-ray diffractograms of the iron aluminate-based powders following synthesis and the experimental campaign are shown in Figure 1. Superimposed on the plots are the characteristic diffraction peaks of $FeAl_2O_4$ and Fe_3O_4 as denoted by the solid and dashed vertical lines, respectively; the diffraction peaks of the former are located at higher 2Θ values, since the lattice parameters of Fe_3O_4 are larger (i.e., $a = b = c = 8.15$ Å and 8.40 Å for $FeAl_2O_4$ and Fe_3O_4, respectively). Qualitative phase analysis indicates that, after calcination at 1380 °C in a CO/CO_2 atmosphere ($pO_2 \approx 10^{-10}$ bar), the Fe33Al67 sample was primarily composed of the $FeAl_2O_4$ phase, while the Fe47Al53 sample – which exhibits peaks in between the characteristic peaks of each spinel – likely contained a higher proportion of Fe_3O_4. After the experimental campaign, where the samples were exposed to oxygen partial pressures as high as 10^{-2} bar, peaks assigned to corundum and hematite were also observed for both Fe33Al67 and Fe47Al53. Analysis of the Co13Fe20Al67 sample revealed similar behavior: a non-spinel phase (e.g., Al_2O_3) was only observed after subjecting the sample to more oxidizing conditions. Note that for cobalt-containing formulations, the spinel phase may consist of $CoAl_2O_4$, Co_3O_4, $FeAl_2O_4$, and Fe_3O_4; the lattice parameters of $CoAl_2O_4$ and Co_3O_4 are near that of $FeAl_2O_4$ (i.e., $a = b = c = 8.10$ Å and 8.08 Å for $CoAl_2O_4$ and Co_3O_4, respectively).

To quantify the phase composition of, in particular, the Fe33Al67 and Fe47Al53 samples, a multiphase Rietveld refinement of the PXRD data was performed. The calculations, shown as black lines in Figure 1, exhibit close agreement with the observed diffraction patterns as indicated by the final goodness-of-fit (χ^2), which converged to a value less than eight for all refinements. Both iron aluminates were confirmed to be of the spinel phase after calcination and consist of spinel, corundum, and hematite phases after the experimental campaign; the phase compositions and structural refinement parameters are presented in Table 1 and Table S1, respectively. Regarding Fe33Al67, the lattice parameters are close to 8.15 Å (i.e., the value for $FeAl_2O_4$), thus indicating that, as desired, the as-synthesized sample was nearly phase pure. The refinement also indicated that the lattice parameters of the as-synthesized Fe47Al53 sample were larger – a

consequence of a greater amount of Fe_3O_4 (i.e., 26.8 wt. %). After the experimental campaign, the spinel lattice parameters of both samples increased to approximately 8.35 Å, as the proportion of Fe_3O_4 relative to $FeAl_2O_4$ increased. Therefore, although the effects of defects may contribute to changes in peak position, it is evident that the spinel peaks shift to lower 2Θ values as the samples oxidize and the ratio of Fe_3O_4 to other spinels concomitantly increases.[25, 28, 41]

Table 2 presents the elemental compositions of the as-synthesized iron aluminate-based materials, as determined by ICP-OES. These results, which are all near their respective target values, also agree with the elemental compositions calculated from the corresponding phase compositions reported in Table 1. According to the Rietveld refinement, the Fe33Al67 sample consists of 0.34 $mol_{Fe}\ mol_c^{-1}$ and 0.66 $mol_{Al}\ mol_c^{-1}$, while the Fe47Al53 sample consists of 0.48 $mol_{Fe}\ mol_c^{-1}$ and 0.52 $mol_{Al}\ mol_c^{-1}$. Other characterization results, including PXRD patterns of the samples after air calcination at 850 °C as well as SEM and EDS images, are shown in Figures S2 – S4 of the Supporting Information.

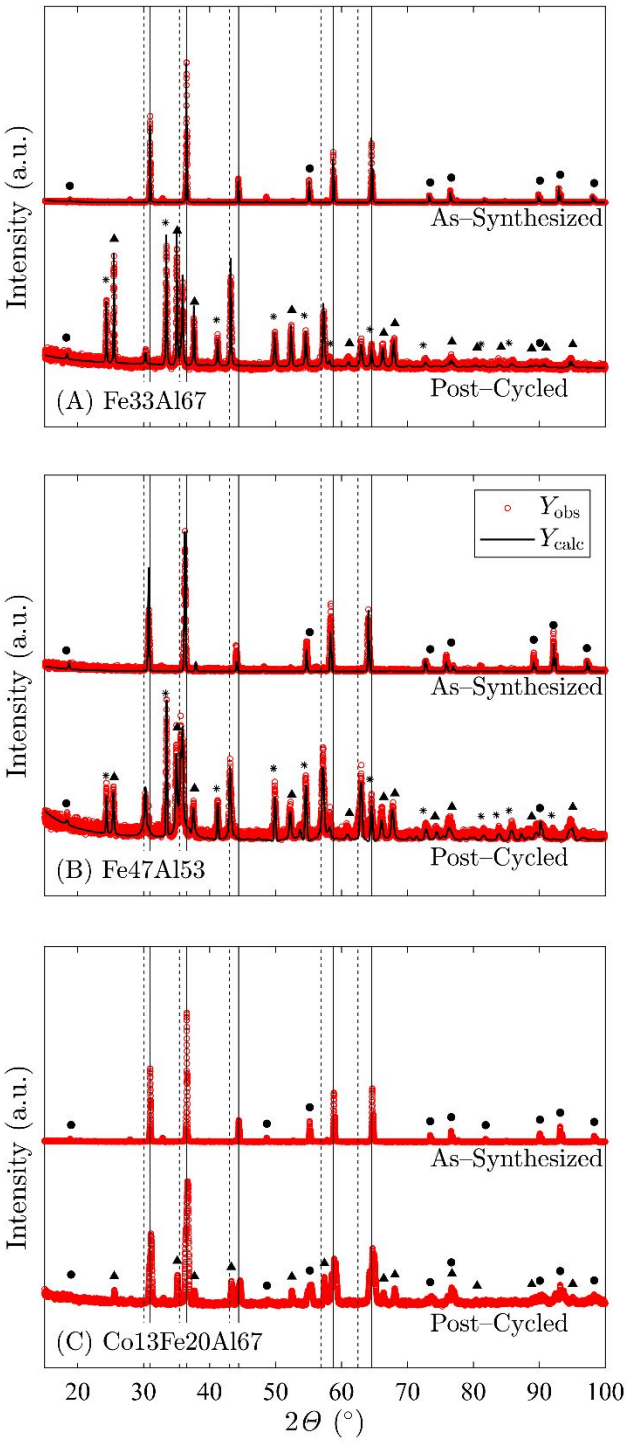

Figure 1. Observed (Y_{obs}) and calculated (Y_{calc}) diffraction patterns of (A) Fe33Al67, (B) Fe47Al53, and (C) Co13Fe20Al67 following synthesis and the experimental campaign. The characteristic diffraction peaks assigned to $FeAl_2O_4$ and Fe_3O_4 are indicated by solid and dashed

vertical lines, while the diffraction peaks assigned to corundum, hematite, and other spinel phases are referred to using triangle (▲), asterisk (□), and circle (●) symbols, respectively.

Table 1. Phase composition (wt. %) of Fe33Al67 and Fe47Al53 following synthesis and the experimental campaign, as determined by multiphase Rietveld refinement.

Phase	Fe33Al67		Fe47Al53	
	As-Synthesized	Post-Cycled	As-Synthesized	Post-Cycled
$FeAl_2O_4$	98.9	4.2	73.2	18.7
Fe_3O_4	1.1	0.6	26.8	9.9
Fe_2O_3	-	24.9	-	20.1
Al_2O_3	-	70.3	-	51.3

Table 2. Elemental composition of the as-synthesized iron aluminate-based materials as determined by ICP-OES.

Element	Co13Fe20Al67		Fe33Al67		Fe47Al53	
	[mg/L]	[mol mol_c^{-1}]	[mg/L]	[mol mol_c^{-1}]	[mg/L]	[mol mol_c^{-1}]
Co	336	0.17	-	-	-	-
Fe	388	0.20	655	0.35	869	0.47
Al	574	0.63	594	0.65	467	0.53

To provide further insight into the results of PXRD and Rietveld refinement, phase diagrams of the Fe-Al-O and Co-Fe-Al-O systems were constructed, as shown in Figure 2. In agreement with previous studies,[38, 39] under the examined conditions, the following phases are present in the Fe-Al-O system: a solid solution (ss) of spinels (i.e., $FeAl_2O_4$ and Fe_3O_4), a solid solution of corundum, a solid solution of hematite, and a solid solution of an intermediate compound (1:1 Fe_2O_3:Al_2O_3). The red region indicates the spinel phase, the blue region indicates the equilibrium of spinel and corundum phases, and the uncolored regions represent the conditions in which the iron aluminates are fully oxidized, as evidenced by the presence of hematite. The solid line between the blue and uncolored regions – which is hereafter referred to as the solid-solution phase boundary – remains constant over a wide range of iron cation compositions (e.g., from 0.125 to 0.5). In contrast, the phase boundary between the red and blue regions shifts towards lower temperatures and higher oxygen partial pressures as ζ increases; the region created by showing the shift in phase boundary (e.g., from $\zeta = 0.35$ to $\zeta = 0.45$ as denoted by the dashed and dot-dashed lines, respectively) is shaded purple, a combination of red and blue, to indicate overlap. In general, the Co-Fe-Al-O system (Figure 2B) exhibits similar behavior, although only three phases are present: a solid solution of spinels (i.e., $CoAl_2O_4$, Co_3O_4, $FeAl_2O_4$, and Fe_3O_4), a solid solution of corundum, and a solid solution of hematite. Here, both phase boundaries – including that between the blue and uncolored regions – change as a function of cobalt cation composition, shifting towards lower temperatures and higher oxygen partial pressures as ζ increases. Thus, the introduction of cobalt in iron aluminates reduces the temperature required for the transition from the oxidized state into a reduced one. The results of these calculations are corroborated by the observations of Figure 1, such as the appearance of corundum and/or hematite in the post-cycled

samples, as the final step of the experimental campaign involved rapid cooling to room temperature under oxygen partial pressures as high as 10^{-2} bar. Note that exemplary PXRD patterns of the samples, when allowed to equilibrate at the fully oxidized state, can be seen in Figure S2.

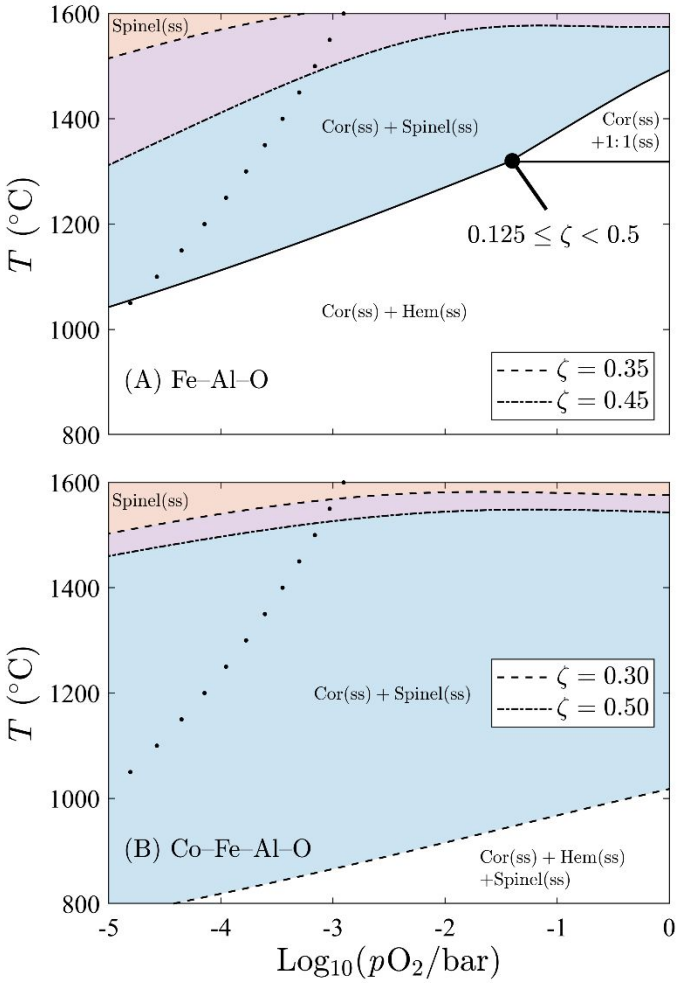

Figure 2. Phase stability of the (A) Fe-Al-O and (B) Co-Fe-Al-O systems as a function of temperature and oxygen partial pressure at select cation compositions. Circle symbols (●) indicate equilibrium oxygen partial pressures that are attainable under water-splitting conditions, as determined according to Equation 6 (i.e., $n_{i,H_2} = 0$), and ζ is defined as $(\mathrm{mol_{Fe}})(\mathrm{mol_{Fe}}+\mathrm{mol_{Al}})^{-1}$ and $(\mathrm{mol_{Co}})(\mathrm{mol_{Co}}+\mathrm{mol_{Fe}})^{-1}$ for the Fe-Al-O and Co-Fe-Al-O systems, where for the latter the aluminum content is 0.67 $\mathrm{mol_{Al}\ mol_c^{-1}}$.

Figures 1 and 2 indicate that, contrary to previous claims,[23, 24, 35, 36] the redox behavior of iron aluminate-based materials cannot be solely attributed to hercynite or a mixed cobalt-iron aluminate compound. Otherwise, phase-pure hercynite, although metastable under ambient conditions, would not rapidly revert back to its original constituents (i.e., Fe_2O_3 and Al_2O_3) once exposed to a sufficiently oxidizing environment at elevated temperatures. Instead, under conditions relevant to the isothermal dissociation of H_2O (see symbols in Figure 2), iron aluminate-based

materials exist as a solid solution composed primarily of magnetite and hercynite spinels. While magnetite is individually incapable of producing appreciable amounts of hydrogen (see Figure S1),[28] when combined with hercynite, the altered equilibrium of the solid solution notably enables water splitting. This phenomenon – a consequence of the change in Gibbs free energy due to mixing – is analogous to the effect of inert zirconia on the thermodynamic properties of ceria; namely, ceria-zirconia solid solutions exhibit markedly greater extents of reduction than that of undoped ceria.[57]

Therefore, in accordance with the established defect structure of iron oxides at high oxygen activities,[40] we assign cation – not oxygen – vacancies as the predominant point defect responsible for the water-splitting ability of iron aluminate-based materials. The general chemical reaction for the removal of oxygen (i.e., reduction) from, for example, iron aluminate spinel solid solutions may then be written as shown in Equation 7.

$$\left(\frac{3 - \delta_f}{4}\right)(Fe_\zeta Al_{1-\zeta})_{3-\delta_i}O_4 \leftrightarrow \left(\frac{3 - \delta_i}{4}\right)(Fe_\zeta Al_{1-\zeta})_{3-\delta_f}O_4 + \frac{1}{2}(\Delta\delta)O_2(g) \quad (7)$$

Note that the notation for spinel solid solution is adopted from Nakamura et al.,[58] and δ, the deviation from stoichiometry, is a measure of the concentration of crystal lattice defects, where the subscripts i and f refer to the initial and final states, respectively. To drive this reaction in the forward direction, $\Delta\delta$ – defined as the difference between δ_i and δ_f – must be positive, thus implying that, unlike materials that accommodate oxygen vacancies, the extent of reduction increases with decreasing δ. In other words, the removal of lattice oxygen requires that cation vacancies are consumed, which, as described using Kröger-Vink notation in Equation 8, is compensated by the conversion of neighboring Fe^{3+} cations into Fe^{2+} cations to maintain charge neutrality.[58]

$$2Fe_{Fe}^{\bullet} + V_{Fe}'' + O_O^x \leftrightarrow 2Fe_{Fe}^x + \tfrac{1}{2}O_2(g) \quad (8)$$

According to the law of mass action, if the activity coefficients are assumed to be unity, the lattice species introduced above can be related as follows:

$$K_1(T) = \frac{[Fe_{Fe}^x]^2\sqrt{pO_2/P^\circ}}{[Fe_{Fe}^{\bullet}]^2[V_{Fe}'']} \quad (9)$$

where K_1 is the temperature-dependent equilibrium constant for the reaction presented in Equation 8, and the square brackets denote concentration per lattice molecule.

Although Equation 9 is capable of qualitatively interpreting the bulk nonstoichiometry of iron aluminate spinel solid solutions, in order to more accurately represent the underlying physics, it was necessary to consider the temperature-dependent site preference of lattice species. In the spinel structure, cations (and vacancies) can be coordinated to either four or six oxygen anions, depending on whether a tetrahedral or octahedral site is occupied. The distribution of cations between sites follows the general formula $A_{1-\lambda}B_\lambda(A_{\lambda/2}B_{1-\lambda/2})_2O_4$, where symbols A and B represent divalent (e.g., Fe^{2+}) and trivalent (e.g., Fe^{3+} and Al^{3+}) cations, parentheses denote the octahedral

sublattice, and λ refers to the degree of inversion. At room temperature, magnetite adopts a predominantly inverse ($\lambda = 1$) distribution, while hercynite adopts a predominantly normal ($\lambda = 0$) one; however, as temperature increases, tetrahedral and octahedral cations exchange their lattice sites ($0 < \lambda < 1$) – a consequence of the entropic effect.[59, 60] Herein, the disordering of the spinel structure was described by introducing the following reactions, which are also written in Kröger-Vink notation.

$$\mathrm{Fe}_{\mathrm{Fe}}^{\bullet} + \left(\mathrm{Fe}_{\mathrm{Fe}}^{\mathrm{x}}\right) \leftrightarrow \mathrm{Fe}_{\mathrm{Fe}}^{\mathrm{x}} + \left(\mathrm{Fe}_{\mathrm{Fe}}^{\bullet}\right) \tag{10a}$$

$$\mathrm{Fe}_{\mathrm{Fe}}^{\mathrm{x}} + \left(\mathrm{Al}_{\mathrm{Al}}^{\mathrm{x}}\right) \leftrightarrow \mathrm{Al}_{\mathrm{Fe}}^{\bullet} + \left(\mathrm{Fe}_{\mathrm{Al}}^{\prime}\right) \tag{10b}$$

$$\mathrm{Fe}_{\mathrm{Fe}}^{\bullet} + \left(\mathrm{V}_{\mathrm{Fe}}^{\prime\prime}\right) \leftrightarrow \mathrm{V}_{\mathrm{Fe}}^{\prime\prime} + \left(\mathrm{Fe}_{\mathrm{Fe}}^{\bullet}\right) \tag{10c}$$

To reduce the number of model equations, only exchanges between lattice species with different charges (or oxidation states) were considered,[61, 62] namely a tetrahedral Fe^{3+} with an octahedral Fe^{2+}, a tetrahedral Fe^{2+} with an octahedral Al^{3+}, and a tetrahedral Fe^{3+} with a doubly ionized octahedral vacancy. For each reaction presented in Equation 10, the law of mass action can be similarly applied to relate the concentrations of corresponding lattice species to a unique equilibrium constant; these relationships are shown in Equation 11.

$$\begin{aligned} K_2(T) &= \frac{\left[\mathrm{Fe}_{\mathrm{Fe}}^{\mathrm{x}}\right]\left[\left(\mathrm{Fe}_{\mathrm{Fe}}^{\bullet}\right)\right]}{\left[\mathrm{Fe}_{\mathrm{Fe}}^{\bullet}\right]\left[\left(\mathrm{Fe}_{\mathrm{Fe}}^{\mathrm{x}}\right)\right]} \\ K_3(T) &= \frac{\left[\mathrm{Al}_{\mathrm{Fe}}^{\bullet}\right]\left[\left(\mathrm{Fe}_{\mathrm{Al}}^{\prime}\right)\right]}{\left[\mathrm{Fe}_{\mathrm{Fe}}^{\mathrm{x}}\right]\left[\left(\mathrm{Al}_{\mathrm{Al}}^{\mathrm{x}}\right)\right]} \\ K_4(T) &= \frac{\left[\mathrm{V}_{\mathrm{Fe}}^{\prime\prime}\right]\left[\left(\mathrm{Fe}_{\mathrm{Fe}}^{\bullet}\right)\right]}{\left[\mathrm{Fe}_{\mathrm{Fe}}^{\bullet}\right]\left[\left(\mathrm{V}_{\mathrm{Fe}}^{\prime\prime}\right)\right]} \end{aligned} \tag{11}$$

In addition, the aforementioned chemical reactions must obey the following bulk conservation equations.

Tetrahedral site balance:

$$\left[\mathrm{Fe}_{\mathrm{Fe}}^{\bullet}\right] + \left[\mathrm{Fe}_{\mathrm{Fe}}^{\mathrm{x}}\right] + \left[\mathrm{V}_{\mathrm{Fe}}^{\prime\prime}\right] + \left[\mathrm{Al}_{\mathrm{Fe}}^{\bullet}\right] = 1 \tag{12}$$

Octahedral site balance:

$$\left[\left(\mathrm{Fe}_{\mathrm{Fe}}^{\bullet}\right)\right] + \left[\left(\mathrm{Fe}_{\mathrm{Fe}}^{\mathrm{x}}\right)\right] + \left[\left(\mathrm{V}_{\mathrm{Fe}}^{\prime\prime}\right)\right] + \left[\left(\mathrm{Al}_{\mathrm{Al}}^{\mathrm{x}}\right)\right] + \left[\left(\mathrm{Fe}_{\mathrm{Al}}^{\prime}\right)\right] = 2 \tag{13}$$

Oxygen site balance:

$$\left[\mathrm{O}_{\mathrm{O}}^{\mathrm{x}}\right] = 4 \tag{14}$$

Tetrahedral electroneutrality:

$$\left[\mathrm{Fe}_{\mathrm{Fe}}^{\bullet}\right] + \left[\mathrm{Al}_{\mathrm{Fe}}^{\bullet}\right] = 2\left[\mathrm{V}_{\mathrm{Fe}}^{\prime\prime}\right] \quad (15)$$

Octahedral electroneutrality:

$$\left[\left(\mathrm{Fe}_{\mathrm{Fe}}^{\bullet}\right)\right] = 2\left[\left(\mathrm{V}_{\mathrm{Fe}}^{\prime\prime}\right)\right] + \left[\left(\mathrm{Fe}_{\mathrm{Al}}^{\prime}\right)\right] \quad (16)$$

Mass balance:

$$\left[\left(\mathrm{Al}_{\mathrm{Al}}^{\mathrm{x}}\right)\right] + \left[\mathrm{Al}_{\mathrm{Fe}}^{\bullet}\right] = 3(1 - \zeta) \quad (17)$$

Although evidence of defect associations have been observed in iron oxides, particularly wüstite,[63] the formation of such clusters in the Fe-Al-O system remains unresolved, and thus point defects were assumed to form ideal solutions on their respective sublattices. Together, Equation 9 and Equations 11 through 17 define the model used to describe the redox behavior of iron aluminates under conditions relevant to two-step thermochemical fuel production. For a particular T, $p\mathrm{O}_2$, and ζ, the concentrations of all lattice species can be determined if initial guesses for the standard molar enthalpies (ΔH°) and entropies (ΔS°) that comprise each equilibrium constant (i.e., K_1, K_2, K_3, and K_4) are specified. Consequently, δ_{model} – a summation of the sublattice vacancy concentrations (i.e., $[(\mathrm{V_{Fe}}'')]$ and $[\mathrm{V_{Fe}}'']$) – can be calculated, thus enabling comparisons with experimental data as described in Section 2.2.2. In this study, the reported thermodynamic state quantities were obtained by using fmincon, a sequential quadratic programming (SQP) algorithm available in MATLAB, to manipulate the set of initial guesses until the global minimum of Equation 2 was found. This approach was validated by reproducing existing defect models for the formation of oxygen vacancies in ceria[64] and a doped lanthanum manganite[47] and demonstrating that the results are in excellent agreement with those obtained by previous authors using other methods. Further details are provided in Section S.4 of the Supporting Information.

It is important to note that while the mechanistic insight presented in this section is relevant for cobalt-containing formulations, the methods described in Section S.2 are not capable of quantifying δ without additional information, as both $\mathrm{Co_3O_4}$ and $\mathrm{CoAl_2O_4}$ exist when cobalt-iron aluminates are fully oxidized (see Figure 2). As a result, the proposed defect model was solely developed for the iron aluminates examined herein (i.e., Fe33Al67 and Fe47Al53).

3.2. Thermodynamic Characterization

Figure 3 shows the thermogravimetric response of pelletized Co13Fe20Al67, Fe33Al67, and Fe47Al53 samples when subjected to changes in temperature at different oxygen partial pressures. For each sample, the extent of reduction, expressed as the percent relative change in mass from the fully oxidized state ($\Delta m/m_{\mathrm{i}}$), increased with increasing T_{ref} and decreasing $p\mathrm{O}_2$ as expected; a negative $\Delta m/m_{\mathrm{i}}$ represents mass loss from the removal of oxygen. Furthermore, formulations with greater amounts of iron (i.e., the primary redox-active element) exhibited greater extents of reduction if compared under conditions where spinel solid solutions exist (see Figure 2). Otherwise, as can be seen in Figure 3A for temperatures less than 1400 °C, the iron aluminates Fe33Al67 and Fe47Al53 remained in the fully oxidized state (i.e., a solid solution of corundum and hematite), whereas the cobalt-containing counterpart Co13Fe20Al67 was appreciably reduced – even at temperatures as low as 1000 °C. This unique aspect of the Fe-Al-O system led to slower

kinetics when approaching or crossing the solid-solution phase boundary, especially for Fe33Al67 at low oxygen partial pressures (Figure 3B). As a result, separate experiments were performed to ensure equilibrium was attained at all conditions; an exemplary thermogravimetric response using an altered procedure is presented in Figure S5.

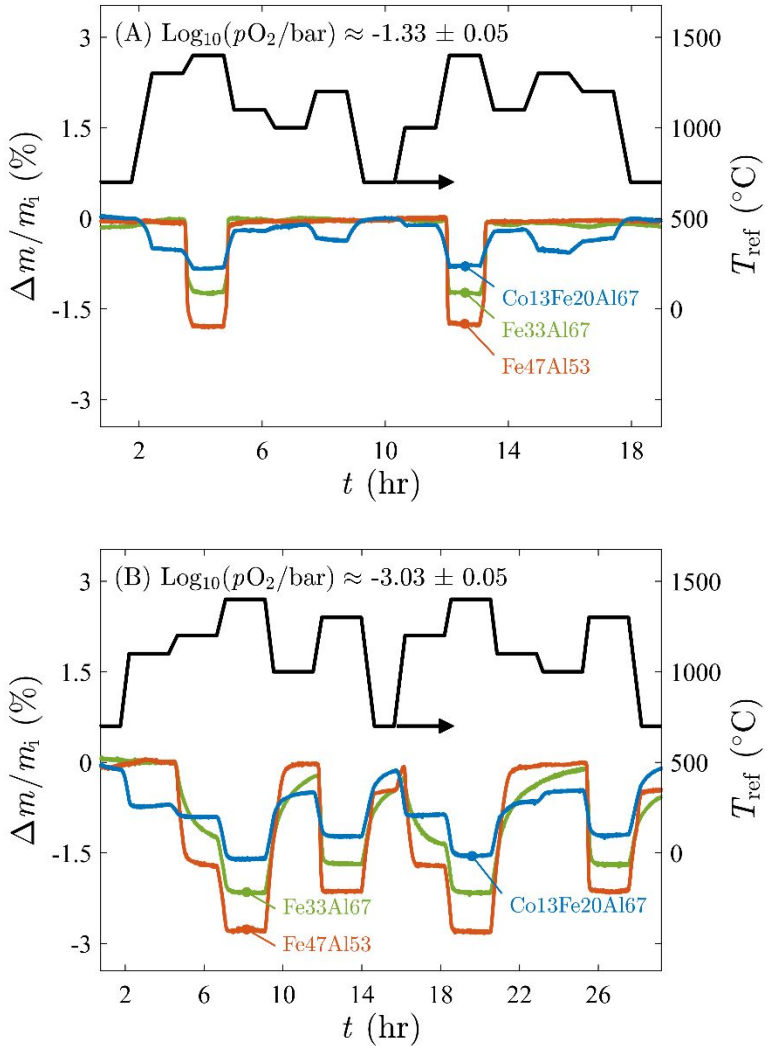

Figure 3. Representative thermogravimetric experiments for establishing the equilibrium behavior of iron aluminate-based materials. Percent relative change in mass from the fully oxidized state (colored lines) and reference temperature (black line) as a function of time at a particular oxygen partial pressure: (A) $p\mathrm{O_2} \approx 4.65\mathrm{x}10^{-2} \pm 5.40\ \mathrm{x}10^{-3}$ bar and (B) $p\mathrm{O_2} \approx 9.39\mathrm{x}10^{-4} \pm 1.08\mathrm{x}10^{-4}$ bar.

The experimental results, such as those displayed in Figure 3 and Figure S5, were evaluated according to the criteria defined in Equation 4 to characterize equilibria as a function of isothermal temperature and oxygen partial pressure; a summation of the equilibrium thermogravimetric measurements is presented in Figure 4. Here, the effect of cation composition on the redox behavior of the samples and, in particular, the location of the solid-solution phase boundary is

further evident. For example, while the equilibrium state of Co13Fe20Al67 is dependent on pO_2 throughout the examined conditions, such dependence is only observed for Fe33Al67 and Fe47Al53 at temperatures above 1100 °C (i.e., once the spinel solid solution phase is established). This phase transition – illustrated in Figure 2 and described by the chemical reaction presented in Equation 18 – is indicated by a significant change in mass over a narrow range of pO_2, as seen for both Fe33Al67 and Fe47Al53 (Figure 4B and 4C, respectively) at 1300 °C between approximately $2x10^{-2}$ and $5x10^{-2}$ bar. Accompanying oxygen evolution is also noticeably greater; representative mass spectrometer measurements are shown in Figure S6.

$$\zeta Fe_2O_3 + (1 - \zeta)Al_2O_3 \leftrightarrow \frac{2}{3 - \delta}(Fe_\zeta Al_{1-\zeta})_{3-\delta}O_4 + \frac{1}{2}\left(\frac{1 - 3\delta}{3 - \delta}\right)O_2(g) \qquad (18)$$

The standard molar enthalpies and entropies used to generate the reported model predictions (solid lines) are listed in Table 3. As expected, regardless of the iron aluminate composition, the defect reactions responsible for the removal of oxygen (Equation 8) and the exchange between tetrahedral Fe^{2+} and octahedral Al^{3+} sites (Equation 10b) are endothermic.[40, 62] Furthermore, the standard molar properties of the latter indicate that – in accordance with the known preference of Al^{3+} for octahedral coordination[58] – the reaction tends towards the left (i.e., $K_3 << 1$ at practicable temperatures). These observations and the close agreement between the experimental data and the thermodynamic (phase diagram and defect model) calculations support the validity of the defect mechanism proposed in Section 3.1., which asserts that the water-splitting ability of iron aluminate-based materials is attributed to (1) the existence of cation vacancies and (2) the interaction of two or more spinels in solid solution. Note that the model is only applicable where the spinel solid solution phase is expected.

To improve figure clarity, since the uncertainties in the oxygen partial pressure and percent relative change in mass are independent of temperature, error bars are only depicted for results at 1400 °C; where not shown, errors are within the size of the symbols. Further details on the methods of estimating measurement uncertainty are provided in Section S.3 of the Supporting Information.

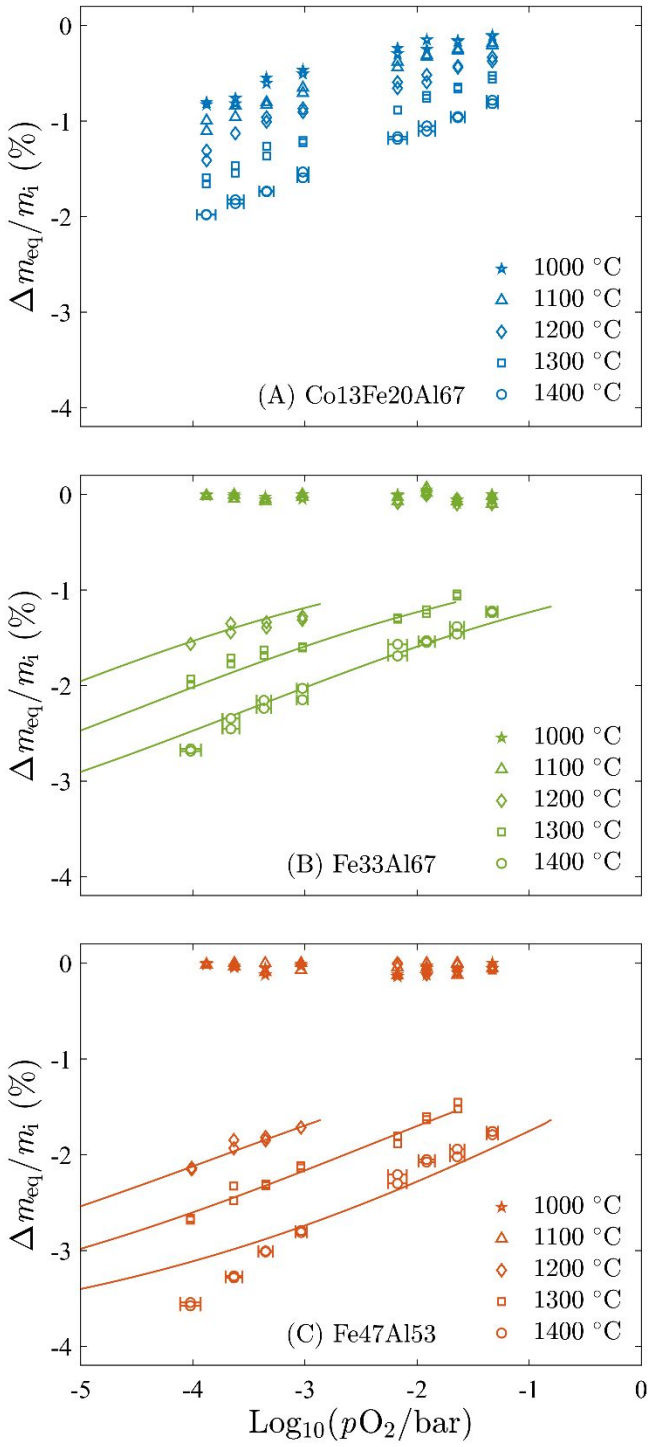

Figure 4. Summation of the thermogravimetric measurements. Percent relative change in mass between the fully oxidized and equilibrium states (symbols) of (A) Co13Fe20Al67, (B) Fe33Al67, and (C) Fe47Al53 as a function of oxygen partial pressure for temperatures between 1000 °C and 1400 °C. Colored lines indicate defect model predictions.

Table 3. Standard molar enthalpy and entropy of the defect reactions associated to cation vacancy consumption and cation exchange in iron aluminate spinel solid solutions.

Equation	Extracted Fitting Parameter	Fe33Al67	Fe47Al53
8	$\Delta\overline{H_1^\circ}$ (kJ mol^{-1})	253.69	321.81
	$\Delta\overline{S_1^\circ}$ (J mol^{-1} K^{-1})	124.09	188.51
10a	$\Delta\overline{H_2^\circ}$ (kJ mol^{-1})	-70.05	-414.88
	$\Delta\overline{S_2^\circ}$ (J mol^{-1} K^{-1})	-20.63	-259.68
10b	$\Delta\overline{H_3^\circ}$ (kJ mol^{-1})	103.45	541.80
	$\Delta\overline{S_3^\circ}$ (J mol^{-1} K^{-1})	-63.19	226.77
10c	$\Delta\overline{H_4^\circ}$ (kJ mol^{-1})	184.67	-241.04
	$\Delta\overline{S_4^\circ}$ (J mol^{-1} K^{-1})	162.14	-143.81

In Figure 5, the equilibrium thermogravimetric measurements and corresponding defect model predictions for Fe33Al67 and Fe47Al53 are displayed with respect to δ and compared with relevant data extracted from literature[40, 65] at 1400 °C. Regardless of the iron aluminate composition, δ (i.e., the extent of oxidation) increases with increasing $p\mathrm{O_2}$, consistent with materials such as magnetite ($\zeta = 1$) that are known to accommodate cation vacancies. For a given $p\mathrm{O_2}$, δ also increases as the proportion of redox-active iron (ζ) decreases, thus affirming that the presence of aluminum constrains the attainable extent of reduction. Notably, only compositions that contain high amounts of aluminum ($\zeta < 0.5$) exhibit the behavior necessary for facilitating water splitting at 1400 °C, namely a positive slope at the equilibrium $p\mathrm{O_2}$ of water thermolysis (in this case, $3.84\text{x}10^{-4}$ bar).

Physically, the formation of cation vacancies is accompanied by the outward diffusion of cations – the phenomenon responsible for the well-known growth of layered scales on iron and iron oxides under highly oxidizing conditions.[66] Under reducing conditions, when cation vacancies are consumed, the direction of cation diffusion shifts inward, and in the limit that, for example, magnetite approaches stoichiometry (i.e., $\delta = 0$) interstitials become the predominant point defect.[40] While multiphase scale growth can be avoided with the introduction of aluminum (due to the formation of stable solid solution phases), the transition from a vacancy-mediated ($\delta > 0$) to an interstitial-mediated ($\delta < 0$) mechanism in magnetite may also occur in iron aluminates and thus explain the discrepancy between the measurements and thermodynamic predictions at low δ.

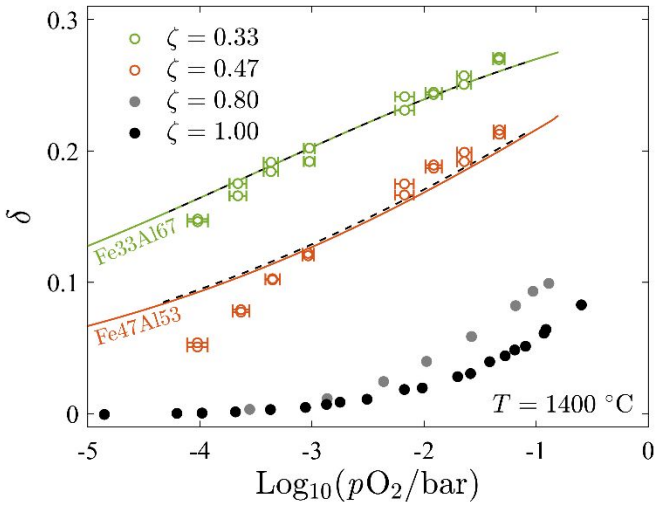

Figure 5. Equilibrium cation nonstoichiometry measurements of iron aluminate spinel solid solutions ($\zeta < 1$) and magnetite ($\zeta = 1$) as a function of oxygen partial pressure at 1400 °C. Open symbols refer to this work, whereas closed symbols refer to data extracted from literature.[40, 65] The solid and dashed lines indicate thermodynamic predictions obtained from evaluating the defect model and Equation 5, respectively.

Defining the standard partial molar enthalpy and entropy of reduction (or oxidation) of a metal oxide allows for the determination of thermodynamic equilibrium at a known T and pO_2, without requiring an understanding of the defect chemistry. An illustration of the procedure to obtain such properties is presented in Figure 6A, which demonstrates that $\Delta\overline{h_v}^\circ$, for example, can be extracted from the slope of the best fit to the model data if plotted according to the linear form of the van't Hoff equation at constant composition. For context, the thermodynamic state functions developed for the reduction of Fe33Al67 and Fe47Al53 are compared in Figure 6B with those previously reported for the reduction of other candidate materials, namely ceria,[67] LSMA6464,[47] and CTM55.[68] In general, the iron aluminates examined in this study exhibit standard partial molar properties that exceed that of the considered perovskites and, at some nonstoichiometries, even surpass that of ceria. This attractive combination of $\Delta\overline{h_v}^\circ$ and $\Delta\overline{s_v}^\circ$ implies that the temperature swing required for each redox reaction to proceed spontaneously is much smaller for the iron aluminates and ceria than that of LSMA6464 and CTM55.[14] While noteworthy, the criteria that a material possesses large enthalpic and entropic changes is not entirely appropriate if the aim is to operate isothermally; here, the material that elicits the largest $\Delta\delta$ within the attainable range of pO_2 (i.e., between 10^{-5} to 10^{-3} bar) will benefit most in terms of efficiency – a consequence of greater fuel yields.[17, 18]

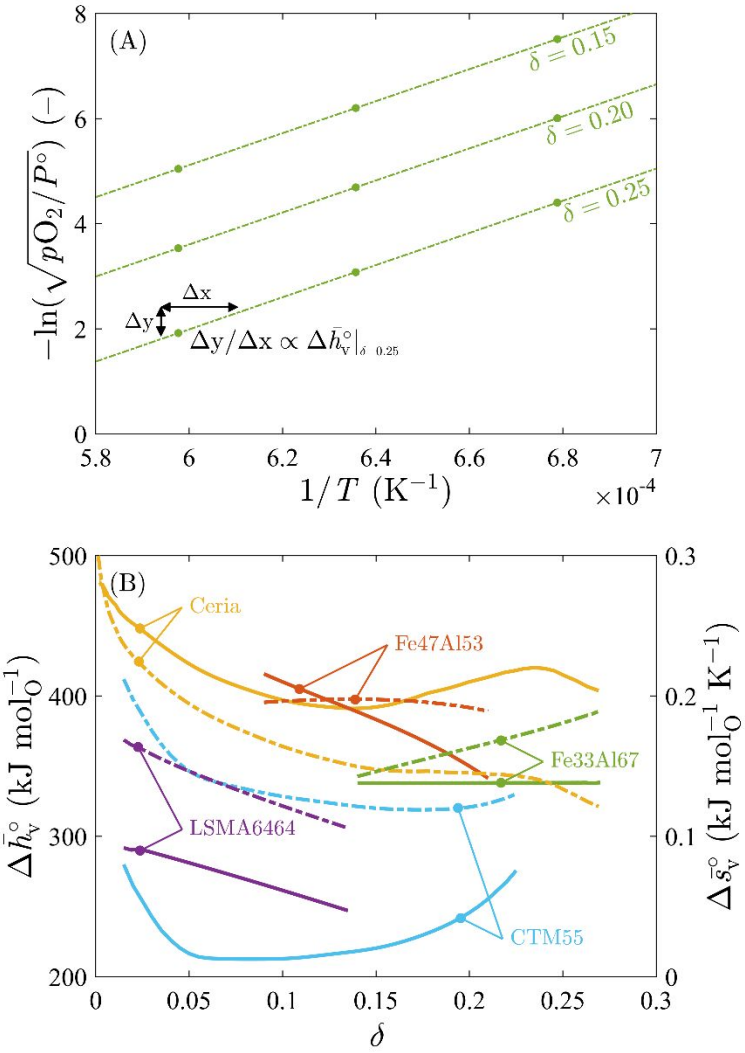

Figure 6. (A) Representative van't Hoff plots, evaluated at select cation nonstoichiometries, for the endothermic reduction of the Fe33Al67 spinel solid solution. (B) Standard partial molar properties (i.e., enthalpy and entropy) for the reduction of several candidate redox materials, namely ceria,[67] LSMA6464,[47] CTM55,[68] and the iron aluminates examined in this study; solid and dot-dashed lines correspond to the left and right ordinate, respectively.

3.3. Water Splitting Efficacy

Figure 7 shows the redox behavior of several candidate materials as a function of oxygen partial pressure at 1400 °C. To ensure a fair comparison, results are expressed as the percent relative change in mass (or oxygen content) between the fully oxidized and equilibrium states, as the interpretation of δ is dependent on the types of defects that a material accommodates. The vertical dot-dashed line represents the maximum pO_2 that is attainable for water splitting at 1400 °C and 1 bar (see Equation 6), and thus, when operating isothermally, the reduction step must be initiated at a lower pO_2 in order to produce hydrogen. Quantifying the cyclic capacity of a material for the production of, in this case, hydrogen involves determining the vertical distance between

the oxygen content at the reduction and oxidation conditions. As a result, for a given T and reduction pO_2, the material with the highest slope (i.e., change in $\Delta m_{eq}/m_i$ per unit change in pO_2) will result in the highest yield. Although the data suggest that the slopes observed for the iron aluminate-based materials increase with increasing iron content, the trend is obscured by the discrepancy between the measurements and thermodynamic predictions at low δ. Therefore, linear approximations (colored dashed lines) were included to provide additional insight at the temperatures evaluated experimentally. Despite this discrepancy, it is evident that the iron aluminate-based materials exhibit slopes that exceed that of ceria and the considered perovskites and are thus more desirable candidates for isothermal redox cycling at 1400 °C.

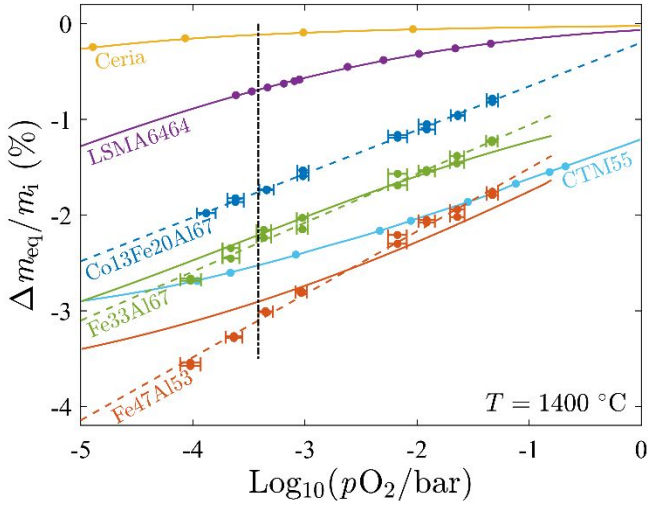

Figure 7. Comparison of the percent relative change in mass, as a function of oxygen partial pressure at 1400 °C, between the fully oxidized and equilibrium states (symbols) of several candidate redox materials, namely ceria,[67] LSMA6464,[47] CTM55,[68] and those examined in this study. Solid and dashed lines indicate thermodynamic predictions and linear approximations, respectively, while the vertical dot-dashed line represents the oxygen partial pressure defined by the equilibrium of water thermolysis at 1 bar (see Equation 6).

The thermochemical water-splitting performance of the candidate redox materials under isothermal conditions is examined in Figure 8. In general, for isothermal operation, the thermodynamic capacity of an oxide for the production of hydrogen (Figure 8A) increases with increasing temperature, as the oxidation pO_2 – determined according to the equilibrium of water thermolysis at 1 bar – concomitantly increases. Notably, the highest capacities are observed for the iron aluminate-based materials, a consequence of possessing partial molar properties that uniquely enable large changes in reaction extent within the attainable range of pO_2 (see Figure 7). At 1400 °C, for example, Fe33Al67 is capable of producing over 450 μmol g^{-1} of hydrogen, whereas LSMA6464 – a perovskite predicted to perform efficiently under isothermal conditions[18] – cannot exceed 370 μmol g^{-1}; the linear approximations suggest that the capacity of Fe47Al53 likely surpasses that of that Fe33Al67. Higher capacities for the production of hydrogen imply that materials are more tolerant of conditions expected in practice, where the amount of steam delivered

must be constrained to reduce sensible heating penalties, and as a result, product hydrogen may not be immediately swept away from the reaction zone. As can be seen in Figure 8B, the materials that exhibit the highest capacities (i.e., the iron aluminate-based materials) are still effective under these "high conversion" conditions,[69] producing over 200 μmol g^{-1} when exposed to oxygen partial pressures as low as that defined by a 500:1 steam-to-hydrogen ratio. Note that increasing the hydrogen yield under less oxidizing atmospheres (i.e., $H_2O:H_2 < 500:1$) is possible if the reduction step is initiated at a lower pO_2; in this comparison, all yields converge at a 200:1 steam-to-hydrogen ratio, as the oxidation pO_2 at this condition is less than that defined for reduction (i.e., 10 ppm residual oxygen). Although the molar conversion of steam to hydrogen is ultimately governed by experimental conditions (i.e., reactor configuration, residence time, reaction duration, etc.), selecting a material with a greater thermodynamic capacity is desirable as – for a given temperature – greater yields can be attained with less oxidant.

To provide further context for the significance of the, for example, iron aluminate performance under isothermal conditions, results are also presented as a function of temperature swing, as shown in Figure 9. For water splitting with high conversion (i.e., $H_2O:H_2 = 500:1$), Fe33Al67 – when operated isothermally at 1400 °C – is capable of exceeding the hydrogen yields of the oxygen vacancy-mediated alternatives following a 400 °C (or less) temperature swing. The examined alternatives include ceria, which is largely recognized as the benchmark material,[2, 10] and CTM55, a recently-developed perovskite marketed as having "outstanding properties" for two-step thermochemical fuel production.[68] Notably, if lower conversion is permitted (e.g., $H_2O:H_2 = 1500:1$), the potential for higher yields with Fe33Al67 is much greater than with ceria, as ceria operates near its fully oxidized state at lower temperatures. The ability to isothermally outperform materials well suited for temperature-swing operation (even under less oxidizing atmospheres) implies that solar-to-hydrogen conversion with iron aluminate-based materials will be more efficient than the conventional approach, as comparable yields are attainable without incurring excessive energy losses from heating and cooling between redox regimes.

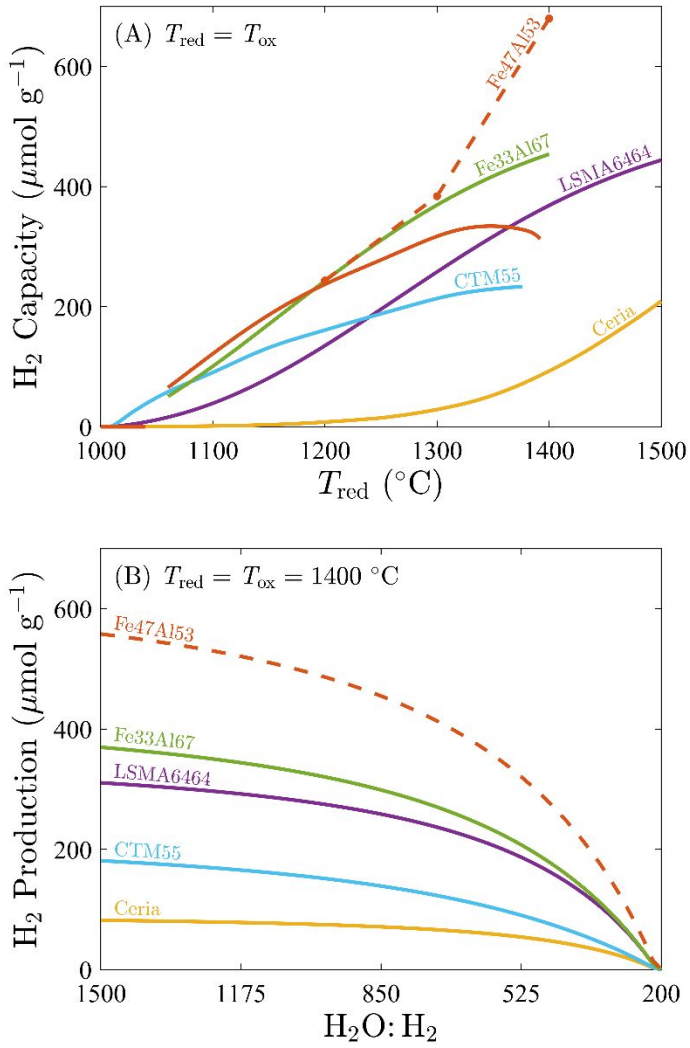

Figure 8. Thermochemical water-splitting performance of several candidate redox materials under isothermal conditions, where the oxidation step is evaluated with (A) pure steam (i.e., H_2O:H_2 = ∞) and (B) steam diluted with product hydrogen (i.e., H_2O:H_2 << ∞). For each calculation, the reduction step is assumed to occur at 1400 °C under an inert atmosphere with 10 ppm residual oxygen, and the product yield is normalized by the mass of the considered material at its stoichiometric state. Solid and dashed lines indicate thermodynamic predictions and linear approximations, respectively.

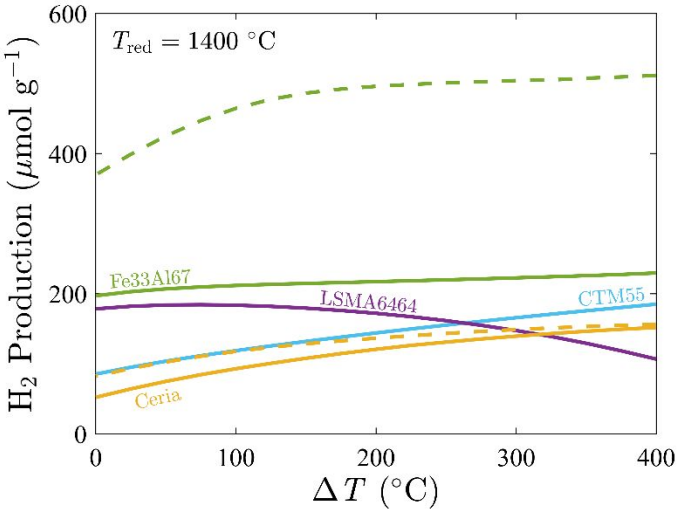

Figure 9. Thermochemical water-splitting performance of several candidate redox materials as a function of temperature swing, where the oxidation step is evaluated under high (i.e., H_2O:H_2 = 500:1) and low (i.e., H_2O:H_2 = 1500:1) conversion conditions[69] as denoted by the solid and dashed lines, respectively. For each calculation, the reduction step is assumed to occur at 1400 °C under an inert atmosphere with 10 ppm residual oxygen, and the product yield is normalized by the mass of the considered material at its stoichiometric state.

An existing stagnation flow reactor[19] was used to evaluate the capacity of Fe33Al67 and ceria under actual thermochemical cycling conditions; the measurements – after accounting for confounding artefacts such as gas-phase thermolysis – are presented in Figure 10. As expected, in accordance with the thermodynamic predictions, Fe33Al67 produced over three times more yield than that of ceria when exposed to the same redox scheme at 1400 °C and 1 bar; the peak reaction rate is also notably higher. Although consistent performance over three thermochemical cycles is insufficient for concluding that the Fe33Al67 is capable of long-term stability, it is worth noting that (1) cobalt-iron aluminates have been previously shown to exhibit no loss in reactivity after over a hundred cycles[70] and (2) degradation of iron-based materials without the presence of aluminum is typically observed following the first cycle.[28]

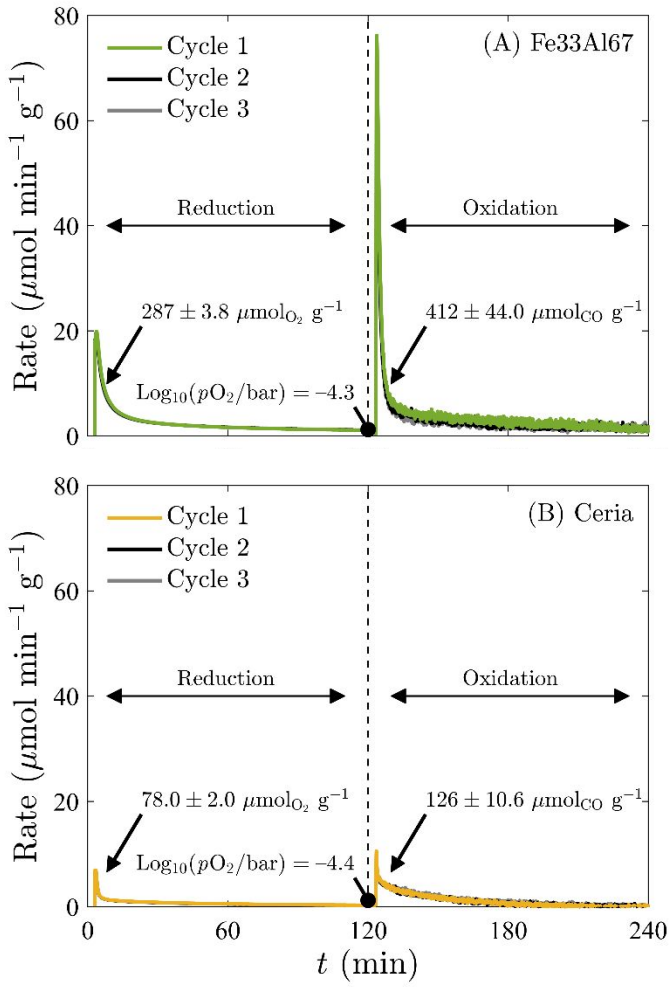

Figure 10. Thermochemical cycling of (A) Fe33Al67 and (B) ceria using a stagnation flow reactor at 1400 °C and 1 bar, where each redox reaction was initiated by delivering either Ar or CO_2 at rate of 500 sccm. Note that three consecutive cycles are overlaid, and the results are normalized by the mass of the considered material at its stoichiometric state (i.e., 4.3 and 10.3 grams for Fe33Al67 and ceria, respectively).

4. Conclusions and Future Outlook

Solar thermochemical water (and/or carbon dioxide) splitting has long been recognized as an efficient approach for full-spectrum solar energy conversion into storable and dispatchable chemical fuels. The commercialization of the conventional, temperature-swing cycle, however, has remained a challenge, as further work is required to (1) develop systems that enable highly effective solid phase heat recovery and (2) ensure that both the active and structural materials can withstand the long-term effects of repetitive changes in temperature. These technological barriers can be avoided by performing each reaction at the same temperature, and thus the isothermal cycle has emerged as a promising alternative to accelerate the realization of fuels produced from solar energy. However, this alternative has yet to be widely adopted, largely due to the perspective that

prohibitive amounts of oxidant are required to drive the exothermic water-splitting reaction at temperatures where it does not occur spontaneously. Moreover, closed-system thermodynamic analyses generally indicate that such processes are most efficient when operated with a temperature swing.[71, 72] These arguments – often biased by considering materials (e.g., ceria) better suited for temperature-swing cycles – do not imply that commercially viable, solar-to-fuel conversion efficiencies cannot be achieved isothermally. Here, efficient operation is contingent on locating a material that exhibits large changes in oxygen content at practical conditions, namely temperatures below 1500 °C and oxygen partial pressures above 10^{-6} bar.

In this study, low-cost iron aluminate-based materials were thoroughly characterized to ascertain the extent of performance under such conditions. Using thermogravimetry, the equilibrium extent of reaction was quantified as a function of cation composition, temperature, and oxygen partial pressure. The measurements were supplemented with a defect model to provide insight into behavior outside the scope of the experimental campaign, as well as clarify previous misconceptions regarding the mechanism by which these materials operate. Guided by X-ray diffraction data and phase equilibrium calculations, the model was based on the observation that, under water-splitting conditions, iron aluminates exist as a solid solution composed primarily of hercynite and magnetite spinels, the latter of which mediates oxygen exchange via cation – not oxygen – vacancies. An open-system thermodynamic analysis further indicated that, unlike pure magnetite, iron aluminate-based spinel solid solutions are capable of splitting water isothermally, a consequence of the change in Gibbs free energy due to mixing. Notably, these materials possess exceptional capacities for the isothermal production of hydrogen and, as a result, remain viable even under high conversion conditions. For example, for water splitting with a steam-hydrogen ratio (i.e., oxygen partial pressure) as low as 500:1, the iron aluminate Fe33Al67 is still capable of producing over 200 μmol g^{-1} of hydrogen at 1400 °C, exceeding the predicted capacities of ceria and two attractive perovskite candidates following a 400 °C (or less) temperature swing. The demonstration of improved performance without requiring excess oxidant and or wide temperature swings represents a leap towards sustainable hydrogen production at scale using only renewable energy sources.

Supporting Information

The Supporting Information is available free of charge at…

Conflicts of Interest

There are no conflicts to declare.

Acknowledgements

This work was supported by the National Science Foundation Graduate Research Fellowship Program under Grant No. DGE-1650115. Use of the analytical equipment in the Nebraska Nanoscale Facility: National Nanotechnology Coordinated Infrastructure and the Nebraska Center for Materials and Nanoscience, which are supported by the National Science Foundation under Award No. ECCS-1542182 and the Nebraska Research Initiative, is greatly appreciated. The

authors also thank Sandy Kanapilly of PerkinElmer for ICP-OES analysis of the as-synthesized samples.

Nomenclature

a, b, c = lattice parameters

$\dot{F}$ = inlet mass flow rate, mol min^{-1}

f = objective function for minimization

K = equilibrium constant

M = molar mass, g mol^{-1}

m = mass, mg

n = number of moles, mol

P° = standard pressure, 1 bar

p = partial pressure, bar

R = universal gas constant, 8.314 J mol^{-1} K^{-1}

T = temperature, °C

t = time, min or hr

Y = intensity

y = mole fraction

Greek

2Θ = diffraction angle, °

Δ = change

$\Delta\bar{G}^{\circ}$ = standard molar Gibbs free energy change, kJ mol^{-1}

$\Delta\bar{H}^{\circ}$ = standard molar enthalpy change, kJ mol^{-1}

$\Delta\bar{S}^{\circ}$ = standard molar entropy change, J mol^{-1}

$\Delta\bar{h_{\mathrm{v}}}^{\circ}$ = standard partial molar enthalpy of reduction, kJ mol^{-1}

$\Delta\bar{s_{\mathrm{v}}}^{\circ}$ = standard partial molar entropy of reduction, kJ mol^{-1} K^{-1}

δ = degree of nonstoichiometry

ε = reaction coordinate

ζ = cation composition

λ = degree of inversion

Subscripts/Superscripts

c = cation

calc = calculated

eq = equilibrium

f = final

i = initial

j = index

obs = observed

ox = oxidation

red = reduction

ref = reference

s = sample

st = stoichiometric sample

v = vacancy

Abbreviations

CTM55 = $CaTi_{0.5}Mn_{0.5}O_3$

Co13Fe20Al67 = $Co_{0.4}Fe_{0.6}Al_2O_4$

DI = deionized

Fe33Al67 = $FeAl_2O_4$

Fe47Al53 = $Fe_{1.4}Al_{1.6}O_4$

LSMA6464 = $La_{0.6}Sr_{0.4}Mn_{0.6}Al_{0.4}O_3$

EDS = energy-dispersive X-ray spectroscopy

FS = full scale

ICP-OES = inductively coupled plasma-optical emission spectrometry

M = measurand

PXRD = powder X-ray diffraction

Rd = reading

TG = thermogravimetric

SEM = Scanning electron microscopy

SQP = Sequential quadratic programming

ss = Solid solution

References

1. A. Steinfeld and R. Palumbo, *Journal*, 2001, **15**, 237-256.
2. W. C. Chueh, C. Falter, M. Abbott, D. Scipio, P. Furler, S. M. Haile and A. Steinfeld, *Science*, 2010, **330**, 1797-1801.
3. S. T. Wismann, J. S. Engbæk, S. B. Vendelbo, F. B. Bendixen, W. L. Eriksen, K. Aasberg-Petersen, C. Frandsen, I. Chorkendorff and P. M. Mortensen, *Science*, 2019, **364**, 756-759.
4. S. C. Rowe, I. Hischier, A. W. Palumbo, B. A. Chubukov, M. A. Wallace, R. Viger, A. Lewandowski, D. E. Clough and A. W. Weimer, *Solar Energy*, 2018, **174**, 474-488.
5. M. E. Dry, *Catalysis today*, 2002, **71**, 227-241.
6. Q. Zhang, W. Deng and Y. Wang, *Journal of Energy Chemistry*, 2013, **22**, 27-38.
7. P. B. Weisz, *PHYSICS TODAY.*, 2004, **57**, 47-52.
8. P. Kreider and W. Lipiński, *Reviews in Mineralogy and Geochemistry*, 2018, **84**, 499-514.
9. T. Nakamura, *Solar energy*, 1977, **19**, 467-475.
10. D. Marxer, P. Furler, M. Takacs and A. Steinfeld, *Energy & Environmental Science*, 2017, **10**, 1142-1149.
11. S. Brendelberger, H. von Storch, B. Bulfin and C. Sattler, *Solar Energy*, 2017, **141**, 91-102.
12. A. A. Emery, J. E. Saal, S. Kirklin, V. I. Hegde and C. Wolverton, *Chemistry of Materials*, 2016, **28**, 5621-5634.
13. B. Meredig and C. Wolverton, *Physical Review B*, 2009, **80**, 245119.
14. R. J. Carrillo and J. R. Scheffe, *Solar Energy*, 2017, **156**, 3-20.
15. B. J. Hathaway, R. Bala Chandran, A. C. Gladen, T. R. Chase and J. H. Davidson, *Energy & Fuels*, 2016.
16. Y. Hao, C.-K. Yang and S. M. Haile, *Physical Chemistry Chemical Physics*, 2013, **15**, 17084-17092.
17. K. Lee, D. C. McCord, R. J. Carrillo, B. Guyll and J. R. Scheffe, *Energy & Fuels*, 2020.
18. R. J. Carrillo and J. R. Scheffe, *Energy & Fuels*, 2019, **33**, 12871-12884.
19. C. L. Muhich, B. W. Evanko, K. C. Weston, P. Lichty, X. Liang, J. Martinek, C. B. Musgrave and A. W. Weimer, *Science*, 2013, **341**, 540-542.
20. P. Lichty, X. Liang, C. Muhich, B. Evanko, C. Bingham and A. W. Weimer, *International journal of hydrogen energy*, 2012, **37**, 16888-16894.
21. J. R. Scheffe, M. D. Allendorf, E. N. Coker, B. W. Jacobs, A. H. McDaniel and A. W. Weimer, *Chemistry of Materials*, 2011, **23**, 2030-2038.
22. C. L. Muhich, B. D. Ehrhart, I. Al-Shankiti and A. W. Weimer, presented in part at the Light, Energy and the Environment, Canberra, 2014/12/02, 2014.
23. S. L. Millican, I. Androshchuk, J. T. Tran, R. M. Trottier, A. Bayon, Y. Al Salik, H. Idriss, C. B. Musgrave and A. W. Weimer, *Chemical Engineering Journal*, 2020, **401**, 126015.
24. C. L. Muhich, B. D. Ehrhart, V. A. Witte, S. L. Miller, E. N. Coker, C. B. Musgrave and A. W. Weimer, *Energy & Environmental Science*, 2015, **8**, 3687-3699.
25. J. P. E. Cleeton, Doctor of Philosophy, University of Cambridge, 2011.
26. P. R. Kidambi, J. P. Cleeton, S. A. Scott, J. S. Dennis and C. D. Bohn, *Energy & fuels*, 2012, **26**, 603-617.

27. W. Liu, M. Ismail, M. T. Dunstan, W. Hu, Z. Zhang, P. S. Fennell, S. A. Scott and J. Dennis, *RSC Advances*, 2015, **5**, 1759-1771.
28. A. Kierzkowska, C. Bohn, S. Scott, J. Cleeton, J. Dennis and C. Muller, *Industrial & Engineering Chemistry Research*, 2010, **49**, 5383-5391.
29. P.-C. Chiu, Y. Ku, Y.-L. Wu, H.-C. Wu, Y.-L. Kuo and Y.-H. Tseng, *Aerosol Air Qual. Res*, 2014, **14**, 981-990.
30. N. S. Yüzbasi, A. Kierzkowska and C. Müller, *Energy Procedia*, 2017, **114**, 436-445.
31. S. J. Roberts, J. J. Dodson, P. L. Carpinone and H. E. Hagelin-Weaver, *International Journal of Hydrogen Energy*, 2015, **40**, 15972-15984.
32. J. Chen, L. Yu, J. Sun, Y. Li and W. Xue, *Journal of the European Ceramic Society*, 2011, **31**, 259-263.
33. J. R. Scheffe, J. Li and A. W. Weimer, *International Journal of Hydrogen Energy*, 2010, **35**, 3333-3340.
34. D. Arifin, V. J. Aston, X. Liang, A. H. McDaniel and A. W. Weimer, *Energy & Environmental Science*, 2012, **5**, 9438-9443.
35. I. A. Al-Shankiti, A. Bayon and A. W. Weimer, *Chemical Engineering Journal*, 2020, **389**, 124429.
36. R. M. Trottier, Z. J. L. Bare, S. L. Millican and C. B. Musgrave, *ACS Applied Materials & Interfaces*, 2020, **12**, 23831-23843.
37. A. L. Hoskins, S. L. Millican, C. E. Czernik, I. Alshankiti, J. C. Netter, T. J. Wendelin, C. B. Musgrave and A. W. Weimer, *Applied Energy*, 2019, **249**, 368-376.
38. C. Meyers, T. O. Mason, W. T. Petuskey, J. Halloran and H. Bowen, *Journal of the American Ceramic Society*, 1980, **63**, 659-663.
39. L. Dreval, T. Zienert and O. Fabrichnaya, *Journal of Alloys and Compounds*, 2016, **657**, 192-214.
40. R. Dieckmann, *Berichte der Bunsengesellschaft für physikalische Chemie*, 1982, **86**, 112-118.
41. A. Turnock and H. Eugster, *Journal of Petrology*, 1962, **3**, 533-565.
42. A. H. McDaniel, *Current Opinion in Green and Sustainable Chemistry*, 2017, **4**, 37-43.
43. P. M. Botta, E. F. Aglietti and J. M. P. López, *Materials chemistry and physics*, 2002, **76**, 104-109.
44. R. J. Harrison, S. A. Redfern and H. S. C. O'Neill, *American Mineralogist*, 1998, **83**, 1092-1099.
45. A. B. Woodland and B. J. Wood, *American Mineralogist*, 1990, **75**, 1342-1348.
46. M. P. Pechini, *Journal*, 1967.
47. M. Takacs, M. Hoes, M. Caduff, T. Cooper, J. Scheffe and A. Steinfeld, *Acta Materialia*, 2016, **103**, 700-710.
48. J. R. Scheffe, R. Jacot, G. R. Patzke and A. Steinfeld, *The Journal of Physical Chemistry C*, 2013, **117**, 24104-24114.
49. T. Cooper, J. R. Scheffe, M. E. Galvez, R. Jacot, G. Patzke and A. Steinfeld, *Energy Technology*, 2015, **3**, 1130-1142.
50. Y.-S. Han and H.-G. Kim, *Journal of power sources*, 2000, **88**, 161-168.
51. R. J. Carrillo, K. J. Warren and J. R. Scheffe, *Journal of Solar Energy Engineering*, 2019, **141**, 021007.
52. M. W. Chase, *Journal*, 1998.

53. S. Gražulis, D. Chateigner, R. T. Downs, A. Yokochi, M. Quirós, L. Lutterotti, E. Manakova, J. Butkus, P. Moeck and A. Le Bail, *Journal of applied crystallography*, 2009, **42**, 726-729.
54. C. Bale, P. Chartrand, S. A. Degterov, G. Eriksson, K. Hack, R. Ben Mahfoud, J. Melancon, A. D. Pelton and S. Petersen, *Calphad*, 2002, **26**, 189-228.
55. K. J. Warren, C. M. Hill, R. J. Carrillo and J. R. Scheffe, *Physical Chemistry Chemical Physics*, 2020, **22**, 8545-8556.
56. M. M. Abbott, J. M. Smith and H. C. Van Ness, *Introduction to Chemical Engineering Thermodynamics*, McGraw-Hill, 2005.
57. Y. Hao, C.-K. Yang and S. M. Haile, *Chemistry of Materials*, 2014, **26**, 6073-6082.
58. A. Nakamura, S. Yamauchi, K. Fueki and T. Mukaibo, *Bulletin of the Chemical Society of Japan*, 1979, **52**, 1019-1026.
59. V. Stevanović, M. d'Avezac and A. Zunger, *Journal of the American Chemical Society*, 2011, **133**, 11649-11654.
60. D. Shishin, V. Prostakova, E. Jak and S. A. Decterov, *Metallurgical and Materials Transactions B*, 2016, **47**, 397-424.
61. T. O. Mason and H. Bowen, *Journal of the American Ceramic Society*, 1981, **64**, 86-90.
62. T. O. Mason, *Journal of the American Ceramic Society*, 1985, **68**, C-74-C-75.
63. J.-R. Gavarri and C. Carel, *Progress in Solid State Chemistry*, 2019, **53**, 27-49.
64. J. R. Scheffe and A. Steinfeld, *Energy & fuels*, 2012, **26**, 1928-1936.
65. S. Yamauchi, A. Nakamura, T. Shimizu and K. Fueki, *Journal of Solid State Chemistry*, 1983, **50**, 20-32.
66. W. Karim, A. Kleibert, U. Hartfelder, A. Balan, J. Gobrecht, J. A. van Bokhoven and Y. Ekinci, *Scientific Reports*, 2016, **6**, 18818.
67. R. Panlener, R. Blumenthal and J. Garnier, *Journal of Physics and Chemistry of Solids*, 1975, **36**, 1213-1222.
68. X. Qian, J. He, E. Mastronardo, B. Baldassarri, W. Yuan, C. Wolverton and S. M. Haile, *Matter*, 2021, **4**, 688-708.
69. D. R. Barcellos, M. D. Sanders, J. Tong, A. H. McDaniel and R. P. O'Hayre, *Energy & Environmental Science*, 2018, **11**, 3256-3265.
70. A. W. Weimer, *Particle Flow Solarthermal Redox Process to Split Water*, United States, 2019.
71. I. Ermanoski, J. Miller and M. Allendorf, *Physical Chemistry Chemical Physics*, 2014, **16**, 8418-8427.
72. I. Al-Shankiti, B. D. Ehrhart and A. W. Weimer, *Solar Energy*, 2017, **156**, 21-29.